RESEARCH

Development of the Arabian-Nubian Shield along the Marsa Alam-Idfu transect, Central-Eastern Desert, Egypt: geochemical implementation of zircon U-Pb geochronology

Sherif Mansour[1*], Noriko Hasebe[2], Kamal Abdelrahman[3], Mohammed S. Fnais[3], Mohamed A. Gharib[1], Rabiou Habou[4*] and Akihiro Tamura[5]

Abstract

The magmatic complex along the Marsa Alam-Idfu transect, Central-Eastern Desert of Egypt, represents the northern segment of the Arabian–Nubian Shield (ANS), which developed within the framework of the East African Orogen. The basement rocks of the Arabian-Nubian Shield have been developed through three distinct phases of magmatic activity: the island-arc, the syn-orogenic, and the post-orogenic phases. Transitioning of the magmatic phases from the syn-orogenic to the post-orogenic, identifies changing the tectonic regime from a compressional to an extensional setting. The scarcity of comprehensive regional geochronological data that rely on precise isochron methods, such as the zircon U-Pb technique, could limit the comprehensive understanding of this region's geological and tectonic history. That would raise a number of uncertainties ranging from the timing of the different magmatic activities and timing of changes in the tectonic regime to the existence of the pre-Pan-African crust in the CED. Our study provides new insights into the aforementioned uncertainties through zircon U-Pb dating of different rock units along the Marsa Alam-Idfu transect, CED, Egypt. The resulting ages ranged from 729±3 Ma to 570±2 Ma, constraining the temporal evolution of the ANS in the studied region into (1) the island-arc phase, represented by a metamorphic sample with an age of 729±3 Ma. (2) the syn-orogenic phase, represented by calc-alkaline and alkaline granitic samples with ages ranging from 699±4 Ma to 646±2 Ma. These two phases indicate initiation of the compressional subduction regime in the CED since 729±3 Ma and being dominated till 646±2 Ma. (3) the post-orogenic phase, represented by metavolcanics, volcanic rocks, and alkaline plutonic samples with ages ranging from 623±3 Ma to 570±2 Ma. This phase suggests dominance of the compressional-to-extensional tectonic transition setting from 623±3 Ma to 600±1 Ma along with the Dokhan volcanism and activation of post-collision tensional regime activated at 582±3 Ma. Our findings discourage the proposed

*Correspondence:
Sherif Mansour
sherif@sci.psu.edu.eg
Rabiou Habou
rabiouhabougarba@yahoo.fr
Full list of author information is available at the end of the article

dominance of the island-arc and syn-orogenic phases in the CED and the classical restriction of older magmatic activity to calc-alkaline granitic rocks and younger magmatic activity to alkaline granitic rocks. Additionally, we identified evidence of local magmatic sources by dating five grains with Mesoproterozoic (pre-Arabian–Nubian Shield) xenocrysts with ages ranging from 1549±4 to 1095±25 Ma.

Keywords Magmatic complex, Zircon U-Pb dating, Arabian-Nubian Shield, Eastern Desert, LA-ICP-MS geochronology

Introduction

The Egyptian Central-Eastern Desert (CED) represents a significant portion of the Arabian-Nubian Shield (ANS), where several temporal-spatial geologic and tectonic characteristics remain uncertain [1–4]. The ANS formed during the East African Orogeny (EAO) between ca. 900 Ma and 550 Ma. This occurred through an amalgamation of the juvenile crust by the accretion of microcontinents and island-arcs into the older continental crust of the Archean age (Fig. 1). Termination of such crustal growth was regionally marked by the development of the Dokhan Volcanics, the Hammamat molasse-sediments, and the Younger granites [5, 6].

Crystalline rocks of the CED consist of the metamorphic gneissose granites and the ophiolitic mélange, which are intruded by several granitic units [4, 7]. Basement rocks with ophiolitic and island-arc affinities are considered to be dominant in the CED [7–12]. Ophiolitic rocks are represented by dismembered serpentinite, gabbro, pyroxenite, and volcanic rocks. The island-arc terranes and the consequent granitic intrusions are traditionally divided into the Older (Gray) granitoids (ca. 800−630 Ma), predominantly comprised of rocks with calc-alkaline chemical compositions, and the Younger (Red) granitoids (ca. 630−540 Ma), primarily composed of alkaline rocks [13–17]. However, recent investigations have revealed the contemporary development of granitoids with both calc-alkaline (Gray granites) and alkaline (Red granites) compositions [2, 18–21]. The timing and tectonic setting of the eruption of the Dokhan Volcanics, occurring towards the ANS's final stages, remain a subject of debate, with differing views suggesting their eruption as a response to either the late-stage collision of East and West Gondwana or the transition between convergent and extensional tectonic settings [6, 22–25].

Early geochronological studies on the ANS basement rocks indicated the presence of pre-Neoproterozoic metamorphic suites predating the East African Orogeny [26–29]. However, more recent studies indicate the lack of any large pre-Neoproterozoic basement [18, 19, 23, 30–39]. Additionally, the timing and tectonic setting of the Dokhan Volcanics, occurring towards the ANS's final stages, remain a subject of debate [6, 22–25].

The reported ages of the basement rocks in the ANS exhibit considerable variability, posing challenges to their classification into established categories [2, 9, 18, 19, 23, 30, 35, 40]. Attempts to delineate distinct intrusive events based on earlier studies face challenges in light of more recent data [22, 30, 34, 41–45]. Additionally, subsequent geological events affected this region with uplift and erosion. These events, including Cambrian thickening-related erosion, Devonian-Carboniferous Variscan tectonic activity, the Cretaceous initiation of the Mid-Atlantic Ridge, and the rifting of the northern Red Sea [46–52], eroded a substantial amount of the basement rocks, and might have removed the majority of the older suites [3].

This study provides new insights into the underlying uncertainties regarding the sequence of the ophiolitic mélange and granitoid emplacement and sorting of the distinct magmatic and volcanic events within the CED. In other words, new constraints on several unresolved critical issues, including the possibility of pre-Neoproterozoic crust existence in the CED, detailed chronological constraints on basement rocks, the tectonic environment of the Dokhan volcanism, and the validity of the classical approach to differentiating magmatic activities based only on a rock's apparent geochemical variations. Our approach to deal with these issues through presenting the precise and well-established zircon U-Pb geochronological results of representative samples from the CED basement that were analyzed using a laser ablation inductively coupled plasma mass spectrometry (LA-ICP-MS) technique (Table 1).

Geologic setting

The term Pan-African Orogeny was first described by Kennedy (53) to describe a sequence of massive tectonic processes extended across the Gondwana supercontinent. The EAO developed the East Africa and Arabian-Nubian Shield as part of the Pan-African tectonism, through the accretion of continental fragments, and ophiolitic and oceanic island-arcs to the Gondwana margin between 870 Ma and 610 Ma [4, 22, 54]. While the ANS represents the northern part of the EAO that is represented in the Egyptian Eastern Desert by calc-alkaline to tholeiitic igneous rocks, metamorphic rocks including gneiss, schist, metavolcanics, metasediments, and ophiolite complexes [10, 55–60].

The temporal evolution of different magmatic and volcanic activities is essential in the geological and tectonic reconstruction of the ANS development. While ages of the ANS basement rocks indicate being formed during the EAO during the Neoproterozoic *[e.g., 1–9]*, pre-EAO
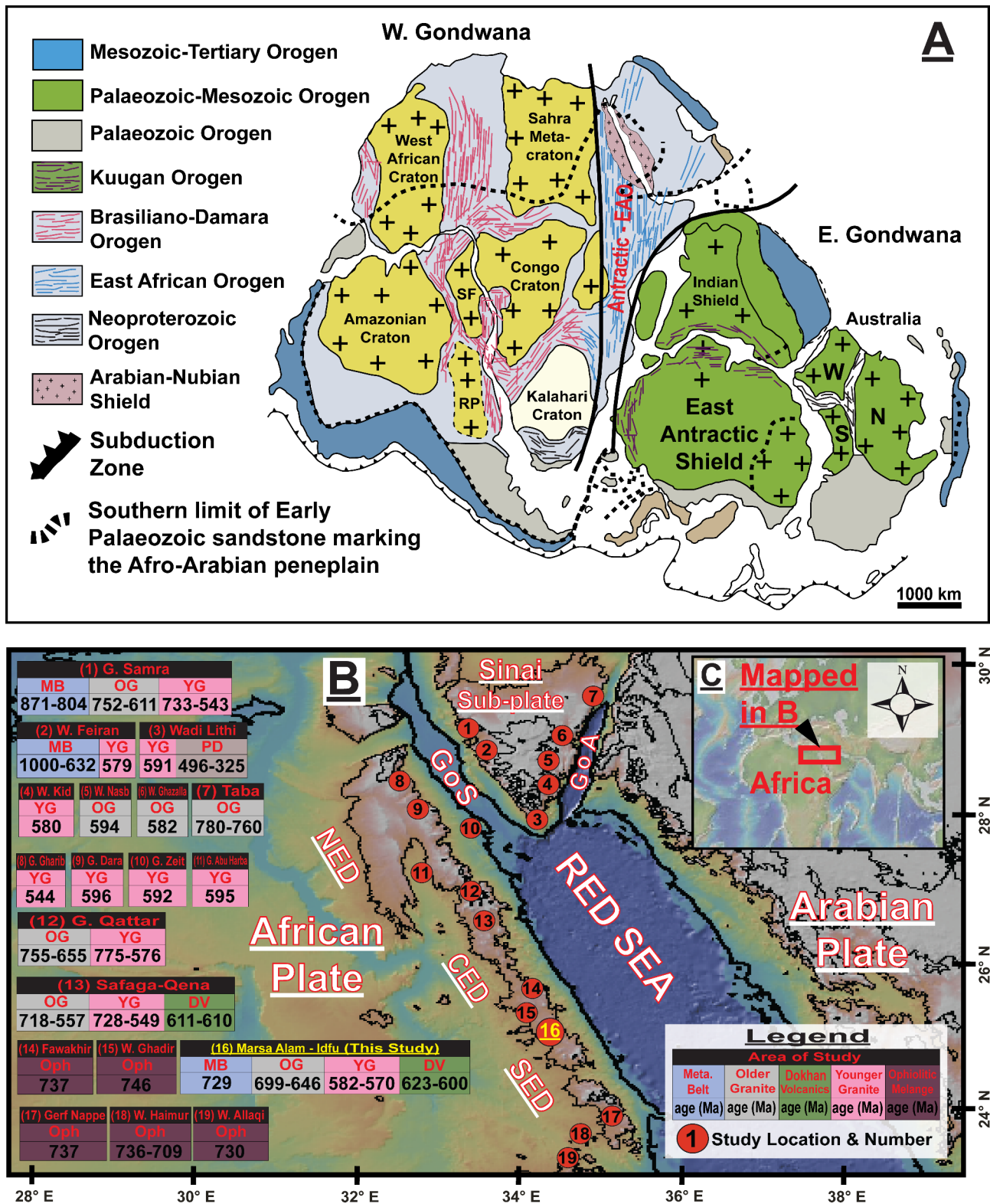
Fig. 1 (**A**) The ANS and the East African Orogen in the context of the Gondwana amalgamation (modified after [132, 133]), . (**B**) Location of northern the ANS (represented in **C**) within the frame of Africa, Arabia, and Eurasia with northern ANS with previous geochronologic studies (modified after [2], . Where, OG is Older Granitoids, YG is Younger Granitoids, PD is Phanerozoic dyke, DV is Dokhan Volcanics, and Oph is ophiolitic sequence. While, G. Samra [2], Feiran area [1, 23, 134], wadi Lithi [135], wadi Kid [136], wadi Nasib and wadi Ghazalla [19], Taba area [20], Gabal Gharib [22], Gabal Dara, Gabal Zeit, Gabal Abu Harba, Gabal Qattar [30, 44], and Fawakhir, W.Ghadir, Gerf Nappe, W. Haimur, and W. Allaqi [35, 40]

Table 1 The samples examined for this study

Sample	Location		Elev.	Rock Type	Traditional Suite Classification	Concordant	
	Lat.	Long.	m.a.s.l.			Age (Ma)	±2σ (Ma)
Island-arc							
MI10	25.06247	33.78872	410	Gneiss	Metamorphic	729.3	2.7
Syn-orogenic							
MI02	25.05656	34.79372	150	Diorite	Older Granite	699.1	4.3
MI11	25.06247	33.78872	401	Syenite	Younger Granite	680.4	5.2
MI03	25.03839	34.74478	246	Granite	Younger Granite	647.2	3.3
MI07	25.0455	34.54231	456	Syenite	Younger Granite	645.9	1.7
Post-orogenic / Dokhan eruptions							
MI04	25.02517	34.69506	323	Meta-andesite	Dokhan Volcanics	623.2	2.7
MI09	25.07892	33.85236	422	Andesite	Dokhan Volcanics	610.9	2.3
MI01	25.05686	34.83792	94	Dacite	Dokhan Volcanics	600.3	1.3
Post-orogenic / Magmatic emplacement							
MI08	25.04558	34.85236	516	Syenogranite	Younger Granite	581.9	2.5
MI06	25.04425	34.56633	475	Syenite	Younger Granite	576.2	1.7
MI05	25.0430	34.5570	488	Granite	Younger Granite	569.8	1.9

Elev. (m.a.s.l.) means elevations in meters above sea level

were reported only from the metamorphic complexes of Sa'al and Feiran-Solaf with ages of ca. 1030−935 Ma [1, 23]. Meanwhile, the youngest ages, from the Younger granites suite, fall between approximately 630 Ma and 580 Ma [2, 8, 19, 20, 30, 41, 61–64]. Tectonically, the compressional regime of the arc-continent collision was dominated between >700−630 Ma, where the final collisional (late-stage subduction) event occurred ca. 630 Ma [65, 66]. While the period between 630 Ma and 580 Ma is considered as a compressional-to-tensional transition period, and the post-collision tensional regime activated<610 Ma [65–67]. The Dokhan Volcanics are divided into two sequences separated by conglomerates and/or an unconformity: (1) an older mafic sequence with basaltic, andesitic, and dacitic compositions and ages ranging between 635−620 Ma [68, 69] and (2) a younger felsic sequence with rhyolitic, rhyodacitic, ignimbritic, and vitric pyroclastics compositions and ages ranging between 618−590 Ma [68, 69]. The timing overlap of the Dokhan eruption and the late subduction to tectonic extension allows for arc subduction and/or within-plate models to explain Dokhan evolution [65, 70]. The petrogenetic studies of the Dokhan suggest development in: (1) a subduction setting [69, 71–73], (2) an extensional setting [74, 75], and (3) a transition setting between subduction and extension [63, 68, 76, 77]. While, a setting of a transitional environment became more popular in recent studies [65]. After ANS construction, subsequent geological events, including the Cambrian thickening-related erosion, the Devonian-Carboniferous Variscan tectonic activity, and the Cretaceous initiation of the Mid-Atlantic Ridge, have eroded a substantial amount of the basement

rocks, especially the older suites, and further reshaped the outcropped rock units [46–51].

The Egyptian Eastern Desert can be broadly divided into three domains, from south to north: the Southern (SED), the Central (CED), and Northern Eastern Desert (NED) regions [22]. The basement rocks of the CED primarily consist of metamorphic, granitoids, and volcanic sequences, which can be broadly categorized into four litho-tectonic units [35]: (1) domal metamorphic and migmatitic sequence, which represents the lower structure unit; (2) the eugeoclinal thrust sheet [35], which consist of the ophiolitic and island-arc assemblages. These rocks are low-grade metamorphic rocks that tectonostratigraphically overlies the Meatiq dome sequence; (3) various volcanics and metasediments of the Dokhan Volcanics and the Hammamat molasse-type sediments, respectively. These unconformably overly the eugeoclinal units; and (4) late- to post-orogenic granitoids, which intrude all the previous units [78–84]. Crystallization ages of these granitoids are essential in the evolution of the Egyptian CED [35, 85].

The domal metamorphic sequence represents the lithostructural lower unit in the CED [14], represented by a series of double plunging asymmetric antiforms [35]. These antiforms signify the ductile root of a major subhorizontal thrust nappe [42], tectonically associated with the Najd Faults System [35, 86]. These domal structures are rimmed by the ophiolites and island-arc sequences. The CED ophiolitic sequence represents the remnants of oceanic crust from the Mozambique Ocean that thrusted over the ANS juvenile crust during the island arc terranes accretion and collisions during the EAO [14, 54, 87, 88]. These ophiolites can be divided into older and younger

metavolcanics that are intruded by subduction-related granitoids [35, 45]. Subsequently, the Dokhan Volcanics erupted between ca. 630 Ma and ca. 590 Ma, exhibiting a range of basic to acidic compositions influenced by the fractional crystallization of basaltic magma and minor crustal contamination [6, 71, 89]. The tectonic setting associated with the Dokhan Volcanics eruptions remains debatable, whether it was activated as a response to the collision of East and West Gondwana or marked the transition between convergent and extensional tectonic settings [6, 22–25]. The granitic intrusions were subdivided based on field observations and bulk chemical compositions into two main groups; (1) an older group (ca. 750–610 Ma) referred to as the "Gray or Calc-alkaline" [90], the Older granites [15], syn- to late-orogenic [2, 14], subduction-related G1 [91], or Gα granites [4] and (2) a younger group (ca. 622–543 Ma) referred to as the Red or Alkaline granites [90], Gattarian [17], Younger granites [15], late-orogenic [2, 92], suture-related G2 [91], or Gβ granites [4]. These classifications do not provide key geochemical or geochronological information, and thus, are difficult to use when assessing the tectonic development of this region in a more detailed manner.

The structural fabric of the CED is concluded in three major deformational events [93]. These are represented by (1) Early NW–SE shortening (D1) associated with the compressional (subduction) tectonic regime associated with the accretion of island arcs and obduction of ophiolites over old continent. D1 produced NNW-directed thrusts and ENE–WSW oriented folds in the CED. These thrusting events were suggested to remain active in CED until ca. 650 Ma at Sibai dome [81, 94, 95], and until ca. 630 Ma at Meatiq and Sibai domes [35]. (2) the D2 structures were developed by changing the tectonic regime from compressional arc-accretion setting to the sinistral transpressional setting at ca. 650 Ma, which was marked by an oblique collision between the Arabian–Nubian Shield and the Nile Craton. This produced NW-trending upright folds, NE-dipping and SW-dipping thrusts, and discreet NW–SE tending shear zones in the CED [93]. (3) the D3 structures were developed during the tectonic transition regime between the compressional and extensional settings between ca. 620 Ma and ca. 580 Ma [93, 96]. The D3 was associated with the exhumation of the CED domal structures, intrusion of gabbroic and granitoid rocks, and development of major NW-trending sinistral shear zones and strike-slip faults related to the Najd fault system [81, 86, 97]. While Andresen et al. (2010) interpreted the D3 deformational event to have resulted from an extensional fault breakaway system. The D3 deformational event was responsible for forming the eugeoclinal rocks, two tectono-metamorphic events, an intervening episode of exhumation and erosion, and emplacement of post-orogenic granites after 630 Ma.

The scarcity and imprecise of many of the available regional geochronological data obscures our knowledge of the ANS geological history. Earlier studies suggested pre-Neoproterozoic basement rocks existence in the Egyptian ANS, but recent geochronological investigations present no conclusive evidence supporting this notion [2, 18, 19, 23, 30–38]. Accordingly, the current consensus is that the basement rocks in the Egyptian ANS are largely Neoproterozoic, with little evidence supporting an older origin.

While data scarcity is an issue, ongoing improvements in geochronological techniques are helping to refine the geological history of the region. Therefore, the temporal and spatial evolution of the different ANS rock units in the CED remains inadequately outlined, and efforts to categorize distinct events require further investigation. Consequently, we conduct the current study, which dates the basement rocks of Marsa Alam-Idfu transect, that signifies the north extent of the western ANS exposures in the Egyptian CED, characterized by the ophiolitic, volcanic, and granitic exposures (Fig. 2).

Methods

Zircon crystals were concentrated using conventional mineral separation techniques such as rock crushing, sieving, Frantz magnetic separator, and heavy liquids. Approximately 100−50 zircon crystals were mounted in a Teflon. Mounted crystals were polished to expose their surfaces. Then, the polished zircon grains were etched in in a NaOH-KOH eutectic melt at 220±5 °C for 60–210 min [2, 34]. The isotopic ratios of U/Pb and Th/Pb were determined using the LA-ICP-MS unit at Kanazawa University, Japan. The LA-ICP-MS instrumental conditions and specifications are presented in Tamura et al. [98] and the applied analytical parameters, including fluence, repetition rate, laser wavelength, spot size, laser fluence, and repetition rate, are summarized in Table 2. Challenges such as the mass bias of the instrument, during-ablation dissociation of U-Th/Pb, and elemental fractionation induced by the laser are common in age dating using the LA-ICP-MS technique. To mitigate these challenges, several approaches were adopted: (1) employing a 213 nm laser wavelength [99, 100]; (2) utilizing a mixture of post-ablation helium and argon gas to carry to the mass spectrometer; (3) limiting the ablation time to ca. 30 s to prevent excessive heating [98, 100–103]; and (4) conducting further measurements of external reference materials such as AS3, GJ1, Fish Canyon, and Plěsovice zircon standards to correct any lasting laser-induced fractionation and minimize instrument mass bias [101, 102].

To obtain a more accurate quantitative analysis of geological samples, the calibration approach should combine the external calibration method with an internal standard
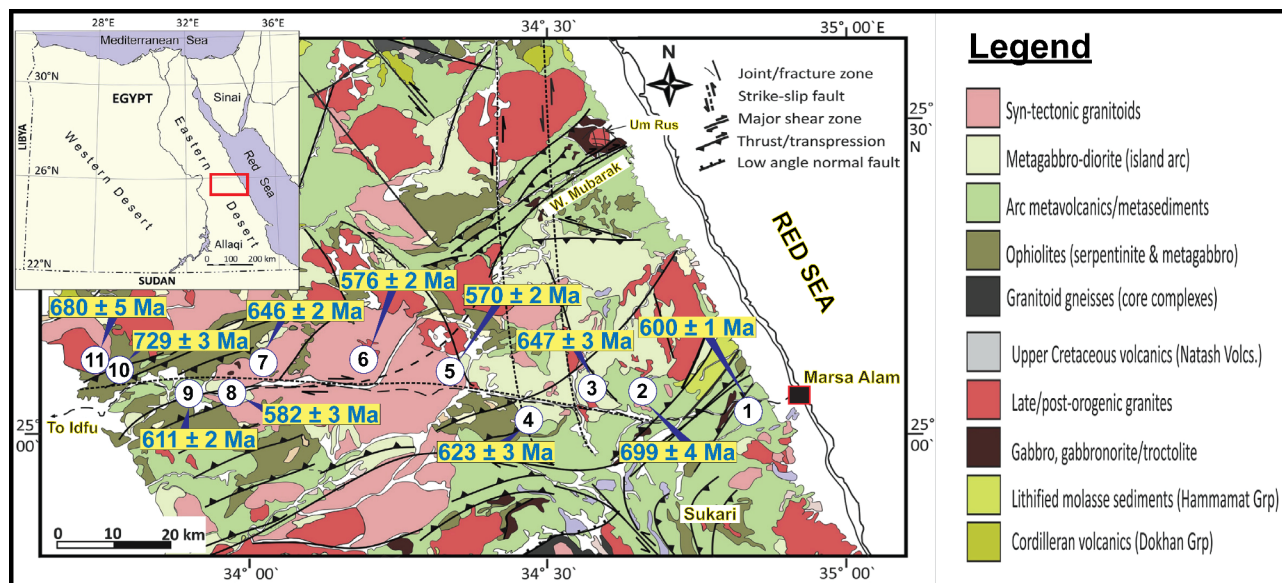
Fig. 2 Geologic map for examined samples along the Marsa Alam-Idfu transect area where samples and their zircon U-Pb ages are represented, and the mapped area eliminated by a red box on the map of Egypt

Table 2 Operating conditions for the LA-ICP-MS

ICP-MS	
Model	Agilent 7850
Forward power	1200 W
Plasma gas flow	15 L min^{-1}
Carrier gas flow	1.10 L min^{-1} (Ar), 0.3 L min^{-1} (He)
Interface	Ni sampler/Ni skimmer
Laser	
Model	UP-213 (New Wave Research)
Wavelength	213 nm (Nd-YAG)
Spot size	25 μm
Repetition rate	5 Hz
Energy density	7 J cm^{-2} (Attenuater: 50–60%)
Warming up	10 s

normalization [104]. The external calibration method is based on the sensitivity obtained by analysis of reference materials containing analyzed elements of known concentrations. The NIST glasses SRM 610 are frequently used as primary calibration standards because they contain many trace elements in high and homogenously distributed concentrations [105]. However, the NIST glasses have the disadvantage of having a completely different matrix from those natural minerals [106–109]. Therefore, the calibration method against multiple external standards with natural composition is preferable [106, 109, 110]. However, they may have some compositional heterogeneities and do not match the range of concentrations expected in the sample for all analyzed elements [105, 110]. Therefore, we have used an integration of analyzing both NIST glasses SRM 610 and multiple natural external standards during our analyses. While, the internal standard calibration method is used to correct for

the elemental fractionation caused by sensitivity drift, matrix effect, and the difference in ablation yield between samples and reference materials [111–114]. Therefore, a calibration approach of combining the external and internal standard calibrations was used routinely during this study to obtain accurate and precise trace element contents by LA-ICP-MS [112, 113]. During this study, zircon reference materials with established chronological origins were regularly analyzed and compared to published data to monitor the precision of our measurements. Sample analyses were frequently sandwiched by the GJ-1 zircon standards analyses with similar analytical conditions. Additionally, isotopic ratios were regularly examined by analyzing different zircon standards with established ages. The produced ages of the zircon standards AS-3, GJ-1, Plěsovice, and Fish Canyon tuff were 1099±2, 612±2, 341±2, and 28.8±0.3 Ma, respectively. These ages overlap with the reference values, which were 1099 Ma [115], 609 Ma [102], 337.1 Ma [116], and 28.4 Ma [117] for AS-3, GJ-1, Plěsovice, and Fish Canyon tuff, respectively. The 238U signal intensities were adjusted using the standard material SRM 610, where the 238U concentration was 456 ppm [118, 119], while, the signal intensity of 29Si was monitored as an internal standard to track the chemical composition of zircon crystals [112, 118].

For each analysis, time-resolved signals were carefully studied to ensure stable flat signal intervals (free from inclusions, core-rim features, and zones with high common Pb or evidence of fractionation). The isotopic ratios after background correction were considered to calculate the average isotopic intensities.

Zircon ages can be corrected for common Pb contamination using different methods [120]. The most common approach involves measuring ^{204}Pb to subtract the common Pb component from the radiogenic Pb isotopes. Still, due to the very low 204 counts (Table 3) (^{204}Pb and ^{204}Hg) and isobaric interference from ^{204}Hg, it was not possible to measure the ^{204}Pb counts with sufficient precision. All age results presented in this work are, therefore, not commonly Pb corrected. The concordant ages and 2σ error, as represented in the text, Fig. 2, and the Concordia diagrams, were calculated using the IsoplotR code [121].

Results

We acquired U-Pb age data from 114 zircon grains belonging to 11 basement rocks, with 10–12 grains from each collected sample. Grains with inclusions or cracks and those exhibiting detectable levels of common ^{204}Pb were excluded. Cathodoluminescence (CL) imaging unveiled diverse internal structures. However, the focus during the analyses was typically directed towards the core to determine the crystallization age (Fig. 3). The percentage of discordance was computed by comparing the ^{206}Pb/^{238}U and ^{207}Pb/^{235}U ages, and grains exceeding 10% discordance were omitted from the calculations. The reported ages and ±2σ error ranges were calculated using IsopltR [121].

Sample MI01 (sample 1 on Fig. 2) is represented by grains that displayed transparency to yellow coloring, were characterized by subhedral faces, and had an average length/width ratio of 2:1. Inclusions were present in approximately 50% of grains, while cracks were observed in approximately 50% of them. The Th/U ratios ranged from 1.1 to 0.17, averaging around 0.46 (Table 3). Grain D7 exhibited discordance exceeding 10% and was therefore disregarded during the age calculations and interpretations. The nine remaining grains displayed concordant ages and formed a single population with a concordant age of 600±1 Ma (Fig. 4). This age was counted as the age of formation of the MI01 dacitic sample (Table 1; Fig. 2).

Sample MI02 (sample 2 on Fig. 2) is represented by grains displaying yellow to brown coloring, were characterized by prismatic shapes with subhedral faces, and had an average length/width ratio of 3:1. Inclusions were present in approximately 50% of the grains, while voluminous cracks were observed in approximately 55% of them. The Th/U ratios ranged from 0.7 to 0.28, averaging around 0.44 (Table 3). Grain F6 exhibited discordance exceeding 10% and was therefore disregarded during the age calculations and interpretations. The nine remaining grains displayed concordant ages, with grain E2 yielding a pre-Pan-African concordant age of 1549±4 Ma and grain E8 yielding an

older concordant age of 723±10 Ma (Fig. 5). The seven remaining grains formed a single population with a concordant age of 699±4 Ma (Fig. 6). This age was counted as the age of formation of the MI02 diorititc sample (Table 1; Fig. 2).

Sample MI03 (sample 3 on Fig. 2) is represented by grains that displayed transparency to yellow coloring, were characterized by equidimensional shapes with euhedral faces, and had an average length/width ratio of 3:1. Inclusions were present in the majority of the grains, while voluminous cracks were observed in approximately 60% of them. The Th/U ratios ranged from 0.48 to 0.16, averaging around 0.31 (Table 3). Grain F5 exhibited discordance exceeding 10% and was therefore disregarded during the age calculations and interpretations. The 11 remaining grains displayed concordant ages and formed a single population with a concordant age of 647±3 Ma (Fig. 6). This age was counted as the age of formation of the MI03 granitic sample (Table 1; Fig. 7).

Sample MI04 (sample 4 on Fig. 2) is represented by grains that displayed transparency to yellow coloring, were characterized by prismatic shapes with subhedral faces, and had an average length/width ratio of 2:1. Inclusions were present in many grains, while voluminous cracks were observed in approximately 50% of them. The Th/U ratios ranged from 1.36 to 0.06, averaging around 0.59 (Table 3). Grains D7 and E7 exhibited discordance exceeding 10% and were therefore disregarded during the age calculations and interpretations. The eight remaining grains displayed concordant ages, with grain D3 yielding a younger concordant age of 594±5 Ma (Fig. 5). The seven remaining grains formed a single population with a concordant age of 623±3 Ma (Fig. 5). This age was counted as the age of formation of the MI04 metavolcanic sample (Table 1; Fig. 2).

Sample MI05 (sample 5 on Fig. 2) is represented by grains displaying yellow to brown coloring, were characterized by prismatic shapes with euhedral faces, and had an average length/width ratio of 3:1. Inclusions and voluminous cracks were observed in approximately 65% of the grains. The Th/U ratios ranged from 0.57 to 0.3, averaging around 0.46 (Table 3). All the ten dated zircon grains displayed concordant ages and formed a single population with a concordant age of 570±2 Ma (Fig. 8), which was counted as the age of formation of the MI05 granitic sample (Table 1; Fig. 2).

Sample MI06 (sample 6 on Fig. 2) is represented by grains that displayed transparency to yellow coloring, were characterized by prismatic shapes with euhedral faces, and had an average length/width ratio of 4:1. Inclusions and

Table 3 LA-ICP-MS U-th-pb Zircon Data for the studied samples

Gr.	Con.		Isotopic ratios and 2σ errors								Age (Ma) and 2σ errors								%discordance
	204Pb	238U	Th/U	±2σ	206Pb/238U	±2σ	207Pb/235U	±2σ	208Pb/232Th	±2σ	206Pb/238U	±2σ	207Pb/235U	±2σ	207Pb/206Pb	±2σ	Conc.	±2σ	
MI01																			
A1	0.006	227	0.640	0.025	0.09783	0.00309	0.81081	0.00280	0.03041	0.00074	602	3	603	3	607	4	603	3	0.2
A3	-0.007	278	0.503	0.021	0.09729	0.00340	0.80593	0.00307	0.03047	0.00073	599	4	600	4	606	5	600	3	0.3
B2	0.001	923	0.170	0.011	0.09795	0.00624	0.81186	0.00566	0.03020	0.00077	602	7	604	6	607	8	604	6	0.2
B5	0.006	528	0.357	0.019	0.09827	0.00473	0.82311	0.00435	0.03070	0.00086	604	6	610	5	629	6	610	5	0.9
C6	0.003	168	1.098	0.041	0.09714	0.00264	0.79830	0.00236	0.03054	0.00084	598	3	596	3	588	4	596	3	-0.3
D1	0.005	279	0.545	0.023	0.09715	0.00340	0.80813	0.00309	0.03037	0.00076	598	4	601	4	615	5	601	4	0.6
*D7	-0.003	839	0.409	0.028	0.05470	0.00326	0.73216	0.00476	0.02446	0.00092	343	4	558	6	1568	6	555	6	38.5
E2	-0.002	713	0.252	0.015	0.09896	0.00554	0.79516	0.00484	0.03053	0.00083	608	7	594	6	539	8	594	6	-2.4
F4	0.001	856	0.241	0.016	0.09759	0.00598	0.80313	0.00537	0.03039	0.00089	600	7	599	6	591	8	599	6	-0.3
G3	-0.005	624	0.315	0.018	0.09791	0.00512	0.80794	0.00462	0.03053	0.00087	602	6	601	5	597	7	601	5	-0.1
MI02																			
A1	0.010	170	0.294	0.009	0.11239	0.00309	0.96840	0.00302	0.03459	0.00050	687	18	688	16	690	19	688	15	0.1
A2	-0.035	223	0.278	0.009	0.11107	0.00350	0.97397	0.00348	0.03457	0.00055	679	20	691	18	727	22	691	17	1.7
C2	-0.003	104	0.497	0.012	0.11175	0.00240	0.98043	0.00239	0.03546	0.00052	683	14	694	12	728	15	694	12	1.6
C5	0.037	286	0.517	0.022	0.11400	0.00407	0.98750	0.00401	0.03528	0.00087	696	24	697	20	702	25	697	20	0.2
D3	0.002	75	0.403	0.008	0.11638	0.00214	1.02708	0.00216	0.03654	0.00041	710	12	717	11	741	13	718	11	1.1
E1	0.004	138	0.696	0.021	0.10784	0.00266	0.92140	0.00255	0.03394	0.00068	660	15	663	13	672	17	663	13	0.4
**E2	0.003	337	0.303	0.013	0.26464	0.01092	3.58033	0.02394	0.08142	0.00171	1514	56	1545	53	1588	37	1549	4	2.0
E8	-0.005	65	0.445	0.009	0.11538	0.00197	1.03792	0.00204	0.03601	0.00040	704	11	723	10	781	12	723	10	2.6
*F6	0.003	26	0.119	0.001	0.15182	0.00165	1.16698	0.00148	0.06947	0.00025	911	9	785	7	441	9	785	7	-16.0
F9	0.004	56	0.539	0.010	0.11384	0.00180	0.98310	0.00176	0.03504	0.00039	695	10	695	9	695	11	695	9	0.0
MI03																			
A1	0.013	562	0.336	0.018	0.10675	0.00532	0.91959	0.00514	0.03435	0.00096	654	16	662	14	690	17	662	13	1.3
A2	0.140	482	0.168	0.008	0.10648	0.00492	0.89714	0.00462	0.03497	0.00064	652	14	650	12	642	16	650	12	-0.3
A8	0.023	258	0.383	0.014	0.10573	0.00357	0.86081	0.00321	0.03471	0.00070	648	10	631	9	568	12	630	9	-2.7
B1	0.064	693	0.334	0.020	0.10357	0.00573	0.87447	0.00537	0.03230	0.00100	635	17	638	15	647	19	638	14	0.4
B8	0.032	729	0.410	0.026	0.1099	0.00625	0.97051	0.00626	0.03540	0.00125	672	18	689	16	742	20	689	16	2.4
C3	0.388	757	0.280	0.017	0.10418	0.00603	0.92454	0.00601	0.03477	0.00103	639	18	665	16	753	19	665	16	3.9
D6	0.085	389	0.273	0.012	0.10206	0.00423	0.84976	0.00388	0.03255	0.00068	626	12	625	11	617	14	625	11	-0.3
E2	0.296	890	0.158	0.010	0.10964	0.00689	0.96367	0.00686	0.03444	0.00083	671	20	685	18	732	22	685	17	2.1
*F5	0.014	1027	0.089	0.006	0.12214	0.00829	0.67413	0.00476	0.04262	0.00083	743	24	523	14	0	26	520	14	-42.0
F9	0.002	541	0.260	0.014	0.10304	0.00503	0.89289	0.00487	0.03450	0.00083	632	15	648	13	702	16	648	13	2.4
G1	0.001	114	0.482	0.013	0.10439	0.00234	0.91455	0.00230	0.03323	0.00050	640	7	659	6	725	8	659	6	2.9
G5	0.002	331	0.281	0.012	0.10169	0.00389	0.84070	0.00354	0.03256	0.00064	624	11	620	10	601	13	619	10	-0.8
MI04																			
A1	0.021	121	0.546	0.015	0.10011	0.00231	0.83616	0.00212	0.03177	0.00052	615	7	617	6	623	8	617	6	0.3

Table 3 (continued)

Gr.	Con. ^{204}Pb	^{238}U	Th/U	±2σ	^{206}Pb/^{238}U	±2σ	^{207}Pb/^{235}U	±2σ	^{208}Pb/^{232}Th	±2σ	^{206}Pb/^{238}U	±2σ	^{207}Pb/^{235}U	±2σ	^{207}Pb/^{206}Pb	±2σ	Conc.	±2σ	%discordance
					Isotopic ratios and 2σ errors						Age (Ma) and 2σ errors								
B5	0.004	449	0.916	0.054	0.10086	0.00448	0.87056	0.00430	0.03289	0.00136	619	13	636	12	694	15	636	12	2.6
C6	-0.007	90	1.362	0.133	0.10221	0.00203	0.83360	0.00182	0.03067	0.00108	627	6	616	5	572	7	616	5	-1.9
C8	-0.009	133	0.697	0.021	0.10049	0.00243	0.84845	0.00227	0.03155	0.00062	617	7	624	6	646	8	624	6	1.0
**D3	0.002	101	0.604	0.015	0.09400	0.00198	0.79424	0.00182	0.03039	0.00048	579	6	594	5	648	7	594	5	2.4
*D7	-0.012	69	1.479	0.039	0.38159	0.00744	3.46731	0.01035	0.05319	0.00110	2084	17	1520	12	802	11	1511	12	-37.1
E2	-0.008	321	0.057	0.002	0.10049	0.00378	0.84982	0.00353	0.03258	0.00028	617	11	625	10	650	13	625	10	1.2
*E7	0.036	134	0.679	0.020	0.18855	0.00475	3.07829	0.01223	0.03360	0.00065	1114	13	1427	15	1932	10	1432	15	22.0
F3	0.061	663	0.305	0.018	0.10170	0.00550	0.86772	0.00520	0.03325	0.00096	624	16	634	14	669	18	634	14	1.6
F7	0.011	175	0.200	0.006	0.10096	0.00280	0.87750	0.00271	0.03231	0.00039	620	8	640	7	709	9	640	7	3.1
MI05																			
A1	-0.006	140	0.372	0.010	0.09361	0.00232	0.85452	0.00234	0.03242	0.00048	577	7	627	6	812	8	627	6	8.0
A8	-0.003	918	0.562	0.043	0.09134	0.00578	0.77329	0.00531	0.02959	0.00136	563	17	582	15	652	20	582	15	3.1
B3	-0.003	158	0.545	0.017	0.08686	0.00228	0.72652	0.00205	0.03004	0.00057	537	7	555	6	626	8	555	6	3.2
B9	0.005	98	0.295	0.007	0.09033	0.00187	0.75206	0.00168	0.03059	0.00033	557	6	569	5	616	7	569	5	2.1
C6	-0.099	182	0.437	0.014	0.08882	0.00250	0.75226	0.00229	0.03064	0.00055	549	7	570	7	653	9	570	7	3.7
C7	0.003	113	0.482	0.012	0.08946	0.00198	0.73852	0.00176	0.02874	0.00043	552	6	562	5	598	7	562	5	1.6
*D2	-0.003	119	0.482	0.013	0.08946	0.00204	0.75368	0.00186	0.02890	0.00044	552	6	570	5	642	7	570	5	3.2
E3	0.002	248	0.353	0.013	0.09452	0.00312	0.76270	0.00272	0.02923	0.00055	582	9	576	8	548	11	576	8	-1.2
F8	0.008	102	0.568	0.014	0.08942	0.00189	0.76056	0.00174	0.02920	0.00045	552	6	574	5	662	7	574	5	3.9
G4	0.003	95	0.535	0.013	0.09056	0.00185	0.77007	0.00170	0.02976	0.00043	559	5	580	5	662	6	580	5	3.6
MI06																			
A1	0.005	43	0.265	0.004	0.09175	0.00126	0.77560	0.00115	0.02822	0.00019	566	4	583	3	649	4	583	3	2.9
A2	0.003	96	0.444	0.010	0.09274	0.00190	0.74702	0.00165	0.02933	0.00039	572	6	566	5	545	7	566	5	-0.9
B5	0.010	345	0.053	0.002	0.09152	0.00355	0.75973	0.00319	0.02940	0.00025	565	10	574	9	610	12	574	9	1.6
B7	0.013	380	0.053	0.002	0.09292	0.00378	0.76981	0.00340	0.02977	0.00027	573	11	580	10	606	13	580	10	1.2
D3	0.004	188	0.804	0.030	0.09690	0.00279	0.79243	0.00248	0.03189	0.00080	596	8	593	7	578	10	593	7	-0.6
D6	0.004	74	0.583	0.013	0.09302	0.00168	0.75203	0.00146	0.02968	0.00040	573	5	569	4	553	6	569	4	-0.7
E2	0.001	104	0.342	0.008	0.08850	0.00189	0.76602	0.00177	0.03054	0.00037	547	6	577	5	700	7	577	5	5.3
*F1	-0.002	37	0.756	0.012	0.09758	0.00125	1.35476	0.00216	0.03677	0.00040	600	4	870	5	1636	4	867	5	31.0
F8	0.008	110	0.424	0.011	0.09843	0.00216	0.80267	0.00192	0.03085	0.00043	605	6	598	5	572	7	598	5	-1.1
G6	-0.002	72	0.428	0.009	0.09131	0.00162	0.73793	0.00141	0.02905	0.00033	563	5	561	4	552	6	561	4	-0.4
MI07																			
A1	-0.010	47	0.509	0.009	0.10609	0.00153	0.89773	0.00145	0.03370	0.00034	650	4	651	4	651	5	651	4	0.1
B2	0.006	103	0.100	0.002	0.10876	0.00232	0.88602	0.00210	0.03488	0.00023	666	7	644	6	569	7	644	6	-3.3
B5	-0.004	77	0.530	0.011	0.10873	0.00201	0.86699	0.00177	0.03357	0.00044	665	6	634	5	522	7	634	5	-5.0
*C8	0.003	70	0.634	0.014	0.11195	0.00197	1.66490	0.00387	0.04440	0.00060	684	6	995	7	1763	5	994	7	31.3
D9	-0.003	31	1.677	0.030	0.11029	0.00129	0.95842	0.00129	0.03444	0.00050	674	4	682	3	708	4	682	3	1.2

Table 3 (continued)

Gr.	Con. 204Pb	Con. 238U	Isotopic ratios and 2σ errors Th/U	±2σ	206Pb/238U	±2σ	207Pb/235U	±2σ	208Pb/232Th	±2σ	Age (Ma) and 2σ errors 206Pb/238U	±2σ	207Pb/235U	±2σ	207Pb/206Pb	±2σ	Conc.	±2σ	%discordance
**E3	-0.045	78	0.583	0.013	0.12569	0.00235	1.09193	0.00237	0.03959	0.00054	763	7	749	6	708	7	749	6	-1.8
E6	0.005	81	0.086	0.002	0.10798	0.00205	0.86268	0.00181	0.03455	0.00019	661	6	632	5	527	7	632	5	-4.7
F6	0.003	43	0.565	0.009	0.10653	0.00146	0.89492	0.00137	0.03500	0.00035	653	4	649	4	636	5	649	4	-0.5
G2	0.004	75	0.290	0.006	0.10435	0.00189	0.90441	0.00184	0.03418	0.00032	640	6	654	5	703	6	654	5	2.2
G7	0.004	64	0.137	0.002	0.10973	0.00185	0.90087	0.00169	0.03458	0.00021	671	5	652	5	586	6	652	5	-2.9
MI08																			
A1	0.005	274	0.545	0.022	0.09665	0.00335	0.77469	0.00291	0.02876	0.00071	595	10	582	8	590	20	582	8	-2.1
A7	-0.002	169	0.546	0.018	0.09339	0.00254	0.78132	0.00231	0.03105	0.00061	576	7	586	7	594	16	586	7	1.8
B2	-0.020	562	0.170	0.009	0.09521	0.00472	0.78224	0.00422	0.02958	0.00059	586	14	587	12	594	14	587	12	0.1
**B4	0.006	165	0.286	0.008	0.12172	0.00331	1.11844	0.00356	0.03906	0.00055	740	10	762	9	772	13	762	9	2.9
B6	-0.001	102	1.098	0.032	0.08991	0.00190	0.71685	0.00162	0.02795	0.00060	555	6	549	5	556	15	549	5	-1.1
B8	0.003	511	0.409	0.022	0.09658	0.00457	0.78904	0.00406	0.03095	0.00091	594	13	591	12	598	25	591	12	-0.6
C7	0.000	128	0.482	0.013	0.09856	0.00234	0.84337	0.00221	0.03161	0.00050	606	7	621	6	629	14	621	6	2.4
D9	-0.001	434	0.252	0.012	0.09690	0.00423	0.80542	0.00384	0.03057	0.00065	596	12	600	11	607	17	600	11	0.6
E1	0.006	380	0.315	0.014	0.09647	0.00394	0.79528	0.00354	0.03022	0.00067	594	12	594	10	602	17	594	10	0.1
E6	-0.012	174	0.536	0.018	0.09459	0.00261	0.77860	0.00233	0.03034	0.00059	583	8	585	7	592	15	585	7	0.4
MI09																			
A1	-0.001	164	0.444	0.014	0.09793	0.00263	0.82906	0.00245	0.03143	0.00055	602	8	613	7	652	9	613	7	1.8
B6	-0.003	396	0.022	0.001	0.09643	0.00402	0.80757	0.00368	0.03120	0.00019	593	12	601	10	629	14	601	10	1.3
C7	0.002	553	0.707	0.043	0.09743	0.00480	0.80835	0.00435	0.03051	0.00122	599	14	602	12	609	16	602	12	0.4
D1	0.001	155	1.409	0.111	0.09992	0.00261	0.87648	0.00254	0.03233	0.00127	614	8	639	7	728	9	639	7	3.9
D3	-0.011	58	0.585	0.011	0.09641	0.00154	0.82322	0.00145	0.03199	0.00038	593	5	610	4	671	5	610	4	2.7
E2	-0.001	113	0.679	0.019	0.09932	0.00221	0.83396	0.00204	0.03148	0.00056	610	6	616	6	635	7	616	6	0.9
E5	0.003	132	0.224	0.006	0.09722	0.00234	0.82142	0.00217	0.03126	0.00035	598	7	609	6	648	8	609	6	1.8
E9	0.007	331	0.378	0.016	0.09776	0.00373	0.82054	0.00343	0.03098	0.00070	601	11	608	10	634	13	608	10	1.2
F2	-0.007	204	0.437	0.015	0.09648	0.00288	0.94217	0.00319	0.02899	0.00055	594	8	674	8	952	9	674	8	11.9
F8	0.002	177	0.546	0.018	0.09789	0.00273	0.83555	0.00256	0.03190	0.00064	602	8	617	7	670	9	617	7	2.4
MI10																			
A1	0.003	80	0.539	0.012	0.11952	0.00226	1.01841	0.00220	0.03623	0.00048	728	6	713	6	666	7	713	6	-2.1
A3	0.001	102	0.043	0.001	0.20585	0.00456	2.09130	0.00632	0.06337	0.00027	1207	12	1146	10	1032	10	1145	10	-5.3
B4	-0.006	148	0.497	0.015	0.11808	0.00304	1.04499	0.00309	0.03830	0.00067	720	9	726	8	747	9	726	8	0.9
B8	0.001	93	0.445	0.010	0.12612	0.00258	1.11339	0.00266	0.03919	0.00051	766	7	760	6	742	7	760	6	-0.8
C1	-0.008	107	0.403	0.010	0.12027	0.00264	1.03970	0.00262	0.03802	0.00051	732	8	724	7	697	8	724	7	-1.2
C3	-0.004	850	0.752	0.058	0.12100	0.00747	1.05150	0.00748	0.03736	0.00192	736	21	730	19	708	22	729	18	-0.9
C5	0.013	242	0.549	0.021	0.10453	0.00342	1.09990	0.00422	0.04492	0.00106	641	10	753	10	1103	10	754	10	14.9
D7	0.002	307	1.128	0.058	0.11747	0.00435	1.07883	0.00435	0.03689	0.00140	716	13	743	11	825	13	743	11	3.6
D8	-0.004	114	0.626	0.017	0.11892	0.00268	1.04414	0.00271	0.03680	0.00063	724	8	726	7	730	8	726	7	0.2

Table 3 (continued)

Gr.	Con.		Isotopic ratios and 2σ errors								Age (Ma) and 2σ errors								%discordance
	^{204}Pb	^{238}U	Th/U	±2σ	$^{206}Pb/^{238}U$	±2σ	$^{207}Pb/^{235}U$	±2σ	$^{208}Pb/^{232}Th$	±2σ	$^{206}Pb/^{238}U$	±2σ	$^{207}Pb/^{235}U$	±2σ	$^{207}Pb/^{206}Pb$	±2σ	Conc.	±2σ	
E5	0.009	173	0.511	0.017	0.19212	0.00551	2.08976	0.00822	0.05954	0.00115	1133	15	1145	14	1168	12	1146	13	1.1
E8	-0.003	181	0.545	0.018	0.19613	0.00576	2.13186	0.00863	0.05985	0.00122	1154	16	1159	14	1167	12	1159	14	0.4
F4	0.005	407	0.517	0.026	0.11798	0.00503	1.04142	0.00511	0.03649	0.00108	719	15	725	13	741	15	725	13	0.8
MI11																			
A1	0.004	158	0.697	0.023	0.10827	0.00287	0.94532	0.00283	0.03596	0.00077	663	17	676	15	718	18	676	15	1.9
A3	0.002	145	0.441	0.013	0.10855	0.00275	0.97064	0.00280	0.03499	0.00057	664	16	689	14	769	17	689	14	3.6
A8	0.004	215	0.674	0.026	0.11104	0.00343	0.93762	0.00326	0.03489	0.00085	679	20	672	17	647	22	672	17	-1.0
B6	-0.008	291	1.128	0.056	0.11234	0.00404	0.97233	0.00397	0.03489	0.00129	686	23	690	20	699	25	690	20	0.6
C2	0.008	196	0.437	0.015	0.17551	0.00533	1.93377	0.00790	0.05648	0.00107	1042	29	1093	24	1194	27	1095	25	4.7
C6	0.000	193	0.608	0.021	0.10948	0.00320	0.96500	0.00320	0.03514	0.00077	670	19	686	17	738	20	686	16	2.3
D8	0.003	209	0.804	0.031	0.10666	0.00324	0.87826	0.00296	0.03446	0.00091	653	19	640	19	592	21	640	16	-2.0
E6	0.008	180	0.295	0.009	0.10982	0.00310	0.97020	0.00311	0.03565	0.00053	672	18	689	16	743	19	689	16	2.5
F2	-0.002	206	0.405	0.014	0.11433	0.00347	0.97192	0.00334	0.03707	0.00069	698	20	689	17	661	21	689	17	-1.3
F6	0.001	130	0.351	0.009	0.14072	0.00343	0.98630	0.00270	0.03648	0.00050	849	19	697	14	232	20	695	14	-21.8

Gr=Grains, A1 grain symbol, *D9 refers to grains with %discordance >10 which were excluded from age calculations, **A9 refers to grains with ages differs from the sample age of population, Conc.= concentration by µg/g, ±2σ error for ^{238}U was calculated from the standard deviation, ±2σ error was calculated for both the isotopic ratios and ages. %discordance is between $^{206}Pb/^{238}U$ and $^{207}Pb/^{235}U$ ages

voluminous cracks were observed in approximately 70% of the grains. The Th/U ratios ranged from 0.8 to 0.05, averaging around 0.38 (Table 3). Grain F1 exhibited discordance exceeding 10% and was therefore disregarded during the age calculations and interpretations. The nine remaining grains displayed concordant ages and formed a single population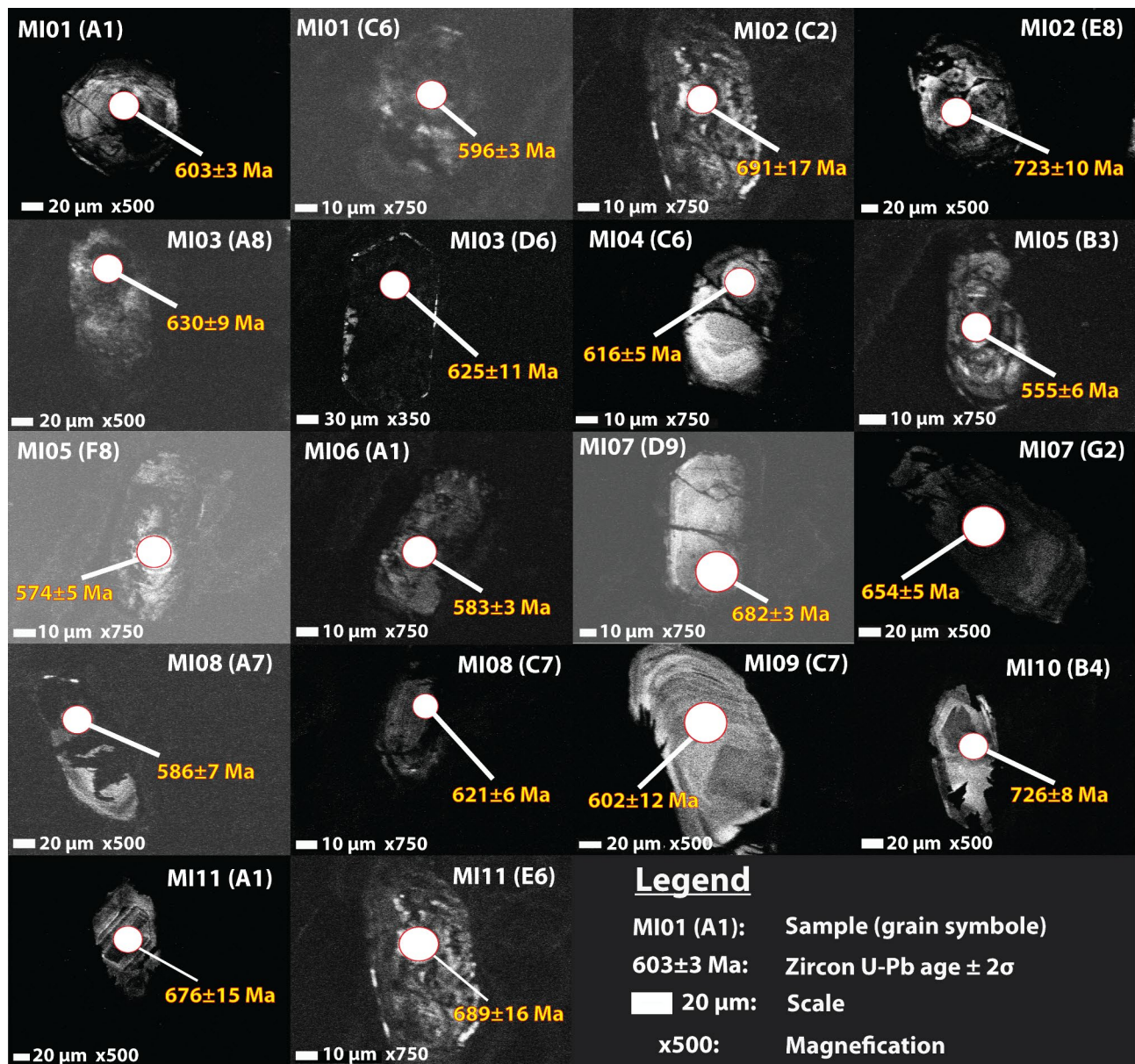 with a concordant age of 576±2 Ma (Fig. 8), which was counted as the age of formation of the MI06 syenitic sample (Table 1; Fig. 2).

Sample MI07 (sample 7 on Fig. 2) is represented by grains that displayed transparency to yellow coloring, were characterized by prismatic shapes with euhedral faces, and had an average length/width ratio of 3:1. Inclusions and voluminous cracks were observed in approximately 75% of the grains. The Th/U ratios ranged from 1.68 to 0.09, averaging around 0.5 (Table 3). Grain C8 exhibited discordance exceeding 10% and was therefore disregarded during the age calculations and interpretations. The nine remaining grains displayed concordant ages, with grain E3 yielding an older concordant age of 749±6 Ma (Fig. 5). The eight remaining grains formed a single population with a concordant age of 646±2 Ma (Fig. 6), which was counted as the age of formation of the MI07 syenitic sample (Table 1; Fig. 2).

Sample MI08 (sample 8 on Fig. 2) is represented by grains displaying yellow to brown coloring, were characterized by prismatic shapes with euhedral faces, and had an average length/width ratio of 3:1. Inclusions and voluminous cracks were observed in approximately 70% of the grains. The Th/U ratios ranged from 1.1 to 0.17, averaging around 0.46 (Table 3). All analysed zircon grains displayed concordant ages, with grains B4 and C7 yielding older concordant ages of 762±9 Ma and 621±6 Ma, respectively (Fig. 5; Table 3). While grain B6 shows a younger concordant age of 549±5 Ma (Fig. 5; Table 3). The seven remaining zircon grains formed a single population with a concordant age of 582±3 Ma (Fig. 8), counted as the age of formation of the MI08 synogranitic sample (Table 1; Fig. 2).

Sample MI09 (sample 9 on Fig. 2) is represented by grains displaying transparent to yellow coloring, were characterized by prismatic shapes with subhedral faces, and had an average length/width ratio of 2:1. Inclusions and voluminous cracks were observed in approximately 55% of the grains. The Th/U ratios ranged from 1.41 to 0.02, averaging around 0.56 (Table 3). Grain F2 exhibited discordance exceeding 10% and was therefore disregarded during the age calculations and interpretations. The nine remaining grains displayed concordant ages and formed a single population with a concordant age of 611±2 Ma

Fig. 3 Cathodoluminescence (CL) images for some of the analyzed zircons, representing location and ages of analyzed spots

(Fig. 5), which was counted as the age of formation of the MI09 andesitic sample (Table 1; Fig. 2).

Sample MI10 (sample 10 on Fig. 2) is represented by grains displaying brown coloring, were characterized by prismatic shapes with euhedral faces, and had an average length/width ratio of 3:1. Inclusions and voluminous cracks were observed in approximately 75% of the grains. The Th/U ratios ranged from 1.13 to 0.04, averaging around 0.55 (Table 3). Grain C5 exhibited discordance exceeding 10% and was therefore disregarded during the age calculations and interpretations. The 11 remaining grains displayed concordant ages, with grains A3, E5, and E8 yielding older concordant ages of 1145±10 Ma,

1146±13 Ma, and 1159±14 Ma (Fig. 5), respectively (Table 3). The eight remaining zircon grains formed a single population with a concordant age of 729±3 Ma (Fig. 6), which was counted as the age of formation of the MI10 gneissic sample (Table 1; Fig. 2).

Sample MI11 (sample 11 on Fig. 2) is represented by grains that displayed transparent to yellow coloring, were characterized by prismatic shapes with euhedral faces, and had an average length/width ratio of 4:1. Inclusions and voluminous cracks were observed in approximately 65% of the grains. The Th/U ratios ranged from 1.13 to 0.3, averaging around 0.61 (Table 3). Grain F6 exhibited discordance exceeding 10% and was therefore disregarded
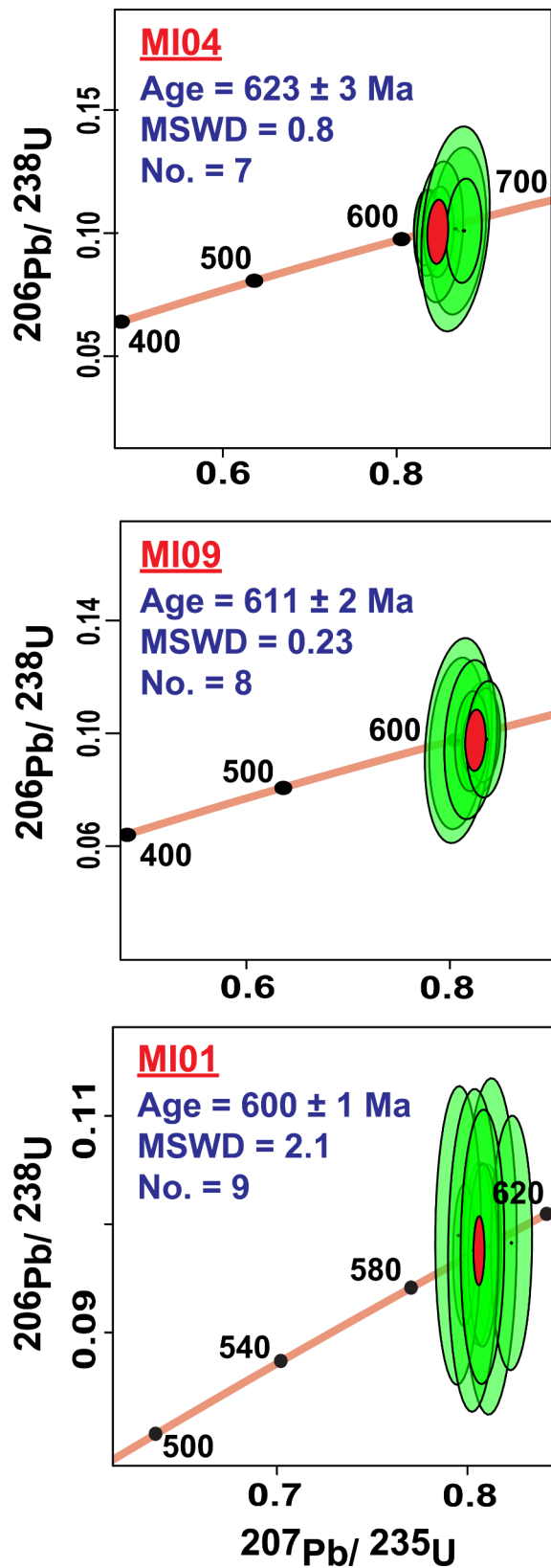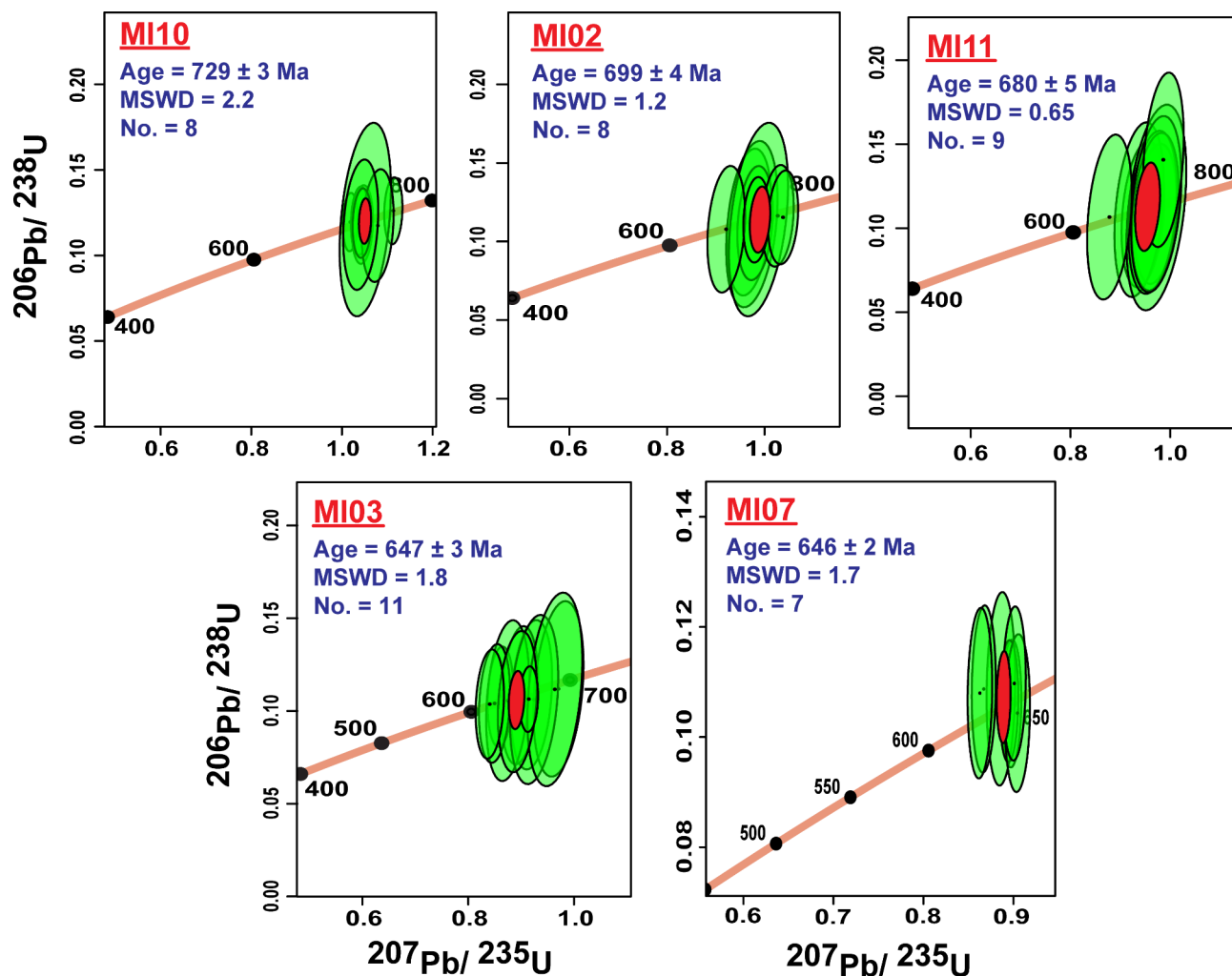
Fig. 4 Concordia diagram for all zircon grains with discordance percent ≤ 10% for Dokhan Volcanics samples, plotted using IsopltR [121]

during the age calculations and interpretations. The nine remaining grains displayed concordant ages and formed a single population with a concordant age of 680±5 Ma (Fig. 6), which was counted as the age of formation of the MI11 syenitic sample (Table 1; Fig. 2).

Discussion

The Th/U ratios across the concordant grains varied between 1.68 and 0.02, averaging ca. 0.48 (Table 3). These ratios aligned with an igneous source [122, 123] for all zircons except for six grains, which exhibited < 0.1 values. These grains were E2 from sample MI04, B5 and B7 from sample MI06, E6 from sample MI07, B6 from sample MI09, and A3 from sample MI10 (Table 3). These were magmatic samples except for samples MI04 and MI10, which were metamorphic rocks (Table 1). However, all six grains were within the age population of their sample (Table 3). The Th/U ratio is usually used as an indicator of the relative depletion or enrichment of U when this ratio is disturbed [124]. However, this might not be the case here as all the aforementioned Th/U ratios are for concordant grains, where any relative depletion or enrichment of the U concentrations would have caused considerable discordance (Table 3).

The reported ages during this study are not corrected for common-lead (^{204}Pb) as their concentrations show low values and are frequently lower than our analytical detection limit (negative values). This would reduce the common-lead potential induced errors and consequently strengthen the reliability of the resulted ages. Additionally, the ^{208}Pb/^{232}Th ages, which are substantially vulnerable to contaminations of common Pb [125], are concordant with the ^{206}Pb/^{238}U ages. These indicate the lack of any effect of common-lead on the produced ages. Any grains displaying discordance > 10% were omitted from their sample's crystallization age calculations and the data assessments (Table 3).

The five concordant zircon grains with pre-Pan-African ages range between 1549±4 Ma and 1095±25 Ma (Table 4; Fig. 5). Although recent geochronological research on the ANS crystalline rocks suggests an absence of any pre-Pan-African units [2, 35, 40, 42, 63, 126, 127], zircon grains with comparable ages have been frequently reported and interpreted as xenocrystic grains [2, 19, 25, 30, 34, 87], suggesting reworked older crust, contaminations of the country rocks, or from a detrital source [128]. These inherited grains are reported from metamorphic and relatively older samples (i.e., MI02, MI10, and MI11). This might support that rock suits with pre-Pan-African ages previously existed and eroded in the studied region [3].

Samples MI02, MI07, and MI08 yielded inherited grains E8 (723±10 Ma), E3 (749±6 Ma), B4 (762±9 Ma), and C7 (621±6 Ma), respectively (Table 4). These grains
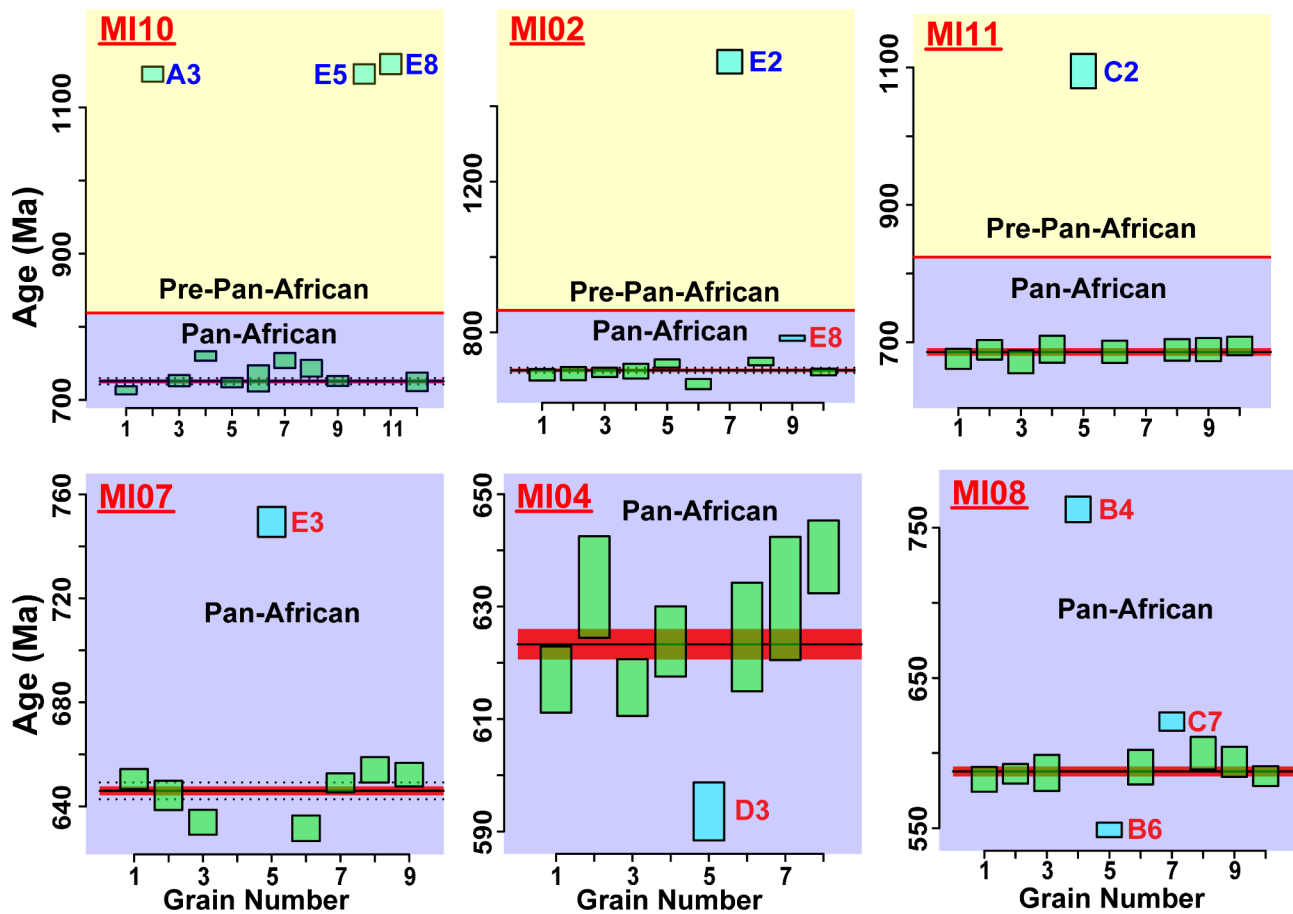
Fig. 5 Single zircon crystals U-Pb ages for samples with pre-Pan-African, Inherited, or younger ages

show older ages than the sample population, consistent with the reported reworked Neoproterozoic crust in the ANS [2, 8, 19, 30, 44]. Grain B6 (549±5 Ma) yielded a younger age than the sample MI08 population, suggesting that it was affected by consequent magmatic events.

The produced zircon U-Pb ages for all samples have Pan-African ages that range between 729±3 Ma and 570±2 Ma (Table 1). The metamorphic sample MI10 yielded the oldest crystallization age of 729±3 Ma, belonging to the second ophiolitic age maxima [60]. This age probably dates to an early stage of the island-arc syn-orogenic phase when the micro-continents convergence into the Archean plates (Fig. 1) during the EAO development in the studied region [2, 35]. Comparable ages have been reported from different parts of the ANS [2, 14, 22, 60, 87, 88, 129, 130]. Andresen et al. [35] reported a comparable age of 736±1 Ma for the sample from the eugeoclinal thrust sheet, which was interpreted as either

the age of the oceanic crust or the volcanic arc [35, 131]. While samples MI02, MI11, MI03, and MI07 yielded ages of 699±4 Ma, 680±5 Ma, 647±3 Ma, and 646±2 Ma, respectively. These samples represent the syn-orogenic stage of the ANS development when a compressional tectonic regime (Convergent) was dominated [2, 22]. These samples are characterized by changing their chemical composition chronologically from the calc-alkaline (diorite) to alkaline (syenite) affinities. This magmatic differentiation from calc-alkaline to alkaline affinities was previously noticed *[e.g., 1–3]*.

The volcanic samples MI04, MI09, and MI01 yielded crystallization ages of 623±3 Ma, 611±2 Ma, and 600±1 Ma, respectively (Table 1). These samples yielded comparable ages to those previously reported from the Dokhan Volcanics [6, 71, 89], marking the initiation of the transition period from compressional-to-extensional tectonic settings [6, 22–25]. All the dated Dokhan
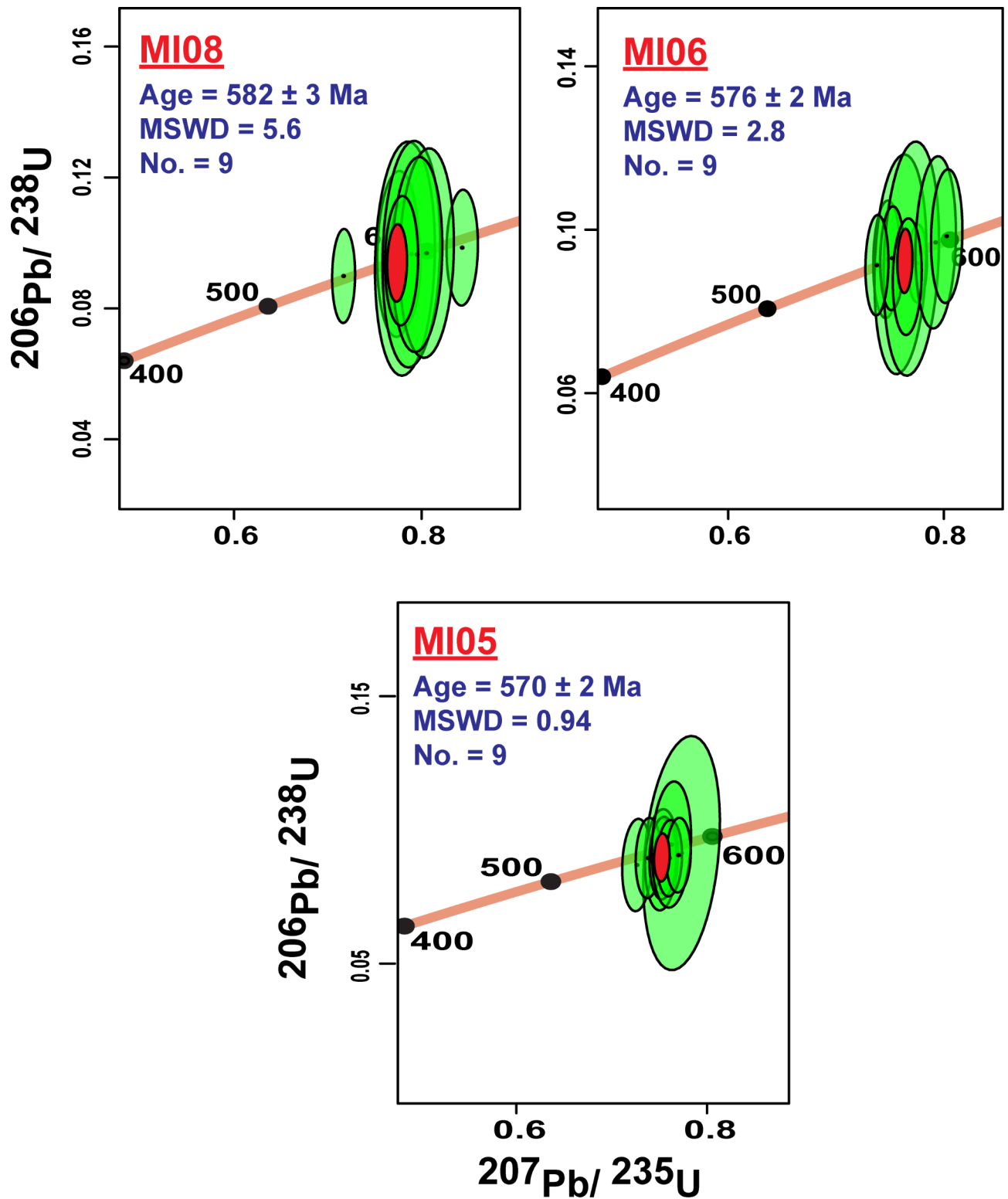
Fig. 6 Concordia diagram for all zircon grains with discordance percent ≤ 10% for island-arc and syn-orogenic samples, plotted using IsopltR [121]

samples should belong to the older mafic Dokhan sequence, which previously dated between 635−620 Ma [68, 69]. Our results suggest extending this phase of volcanism to ca. 600 Ma in the studied region.

The remaining samples, MI08, MI06, and MI05, yielded crystallization ages of 582±3 Ma, 576±2 Ma, and 570±2 Ma, respectively (Table 1). These samples represent magmatic emplacements during the post-orogenic stage of the EAO development in the ANS, where the tensional tectonic regime was dominated [2, 35]. Comparable ages have been reported from different parts of the ANS [2, 14, 22, 60, 87, 88, 129, 130].

Interpretation

The produced zircon U-Pb crystallization ages represent constructing the studied region in the CED through several magmatic pulses: (1) island-arc phase; represented by sample MI10 with an age of 729±3 Ma. (2) syn-orogenic phase; represented by samples MI02 and MI11, MI03, and MI07 with ages of 699±4 Ma, 680±5 Ma, 647±3 Ma, and 646±2 Ma, respectively. These two phases represent the domination of the compressional regime of the arc-continent collision between 729±3 Ma and 646±2 Ma in the region of study. Furthermore, all the dated grains with pre-Pan-African (Paleo- to Meso-Proterozoic) ages belong to these two phases, indicating a probable reworked older crust or contaminations from a detrital source. (3) post-orogenic phase; represented by all other samples. The transition between the compressional syn-orogenic and the extensional post-orogenic tectonic regimes was marked by the eruption of the older mafic Dokhan sequence which extended in the studied region from 623±3 Ma (sample MI04) to 600±1 Ma (sample
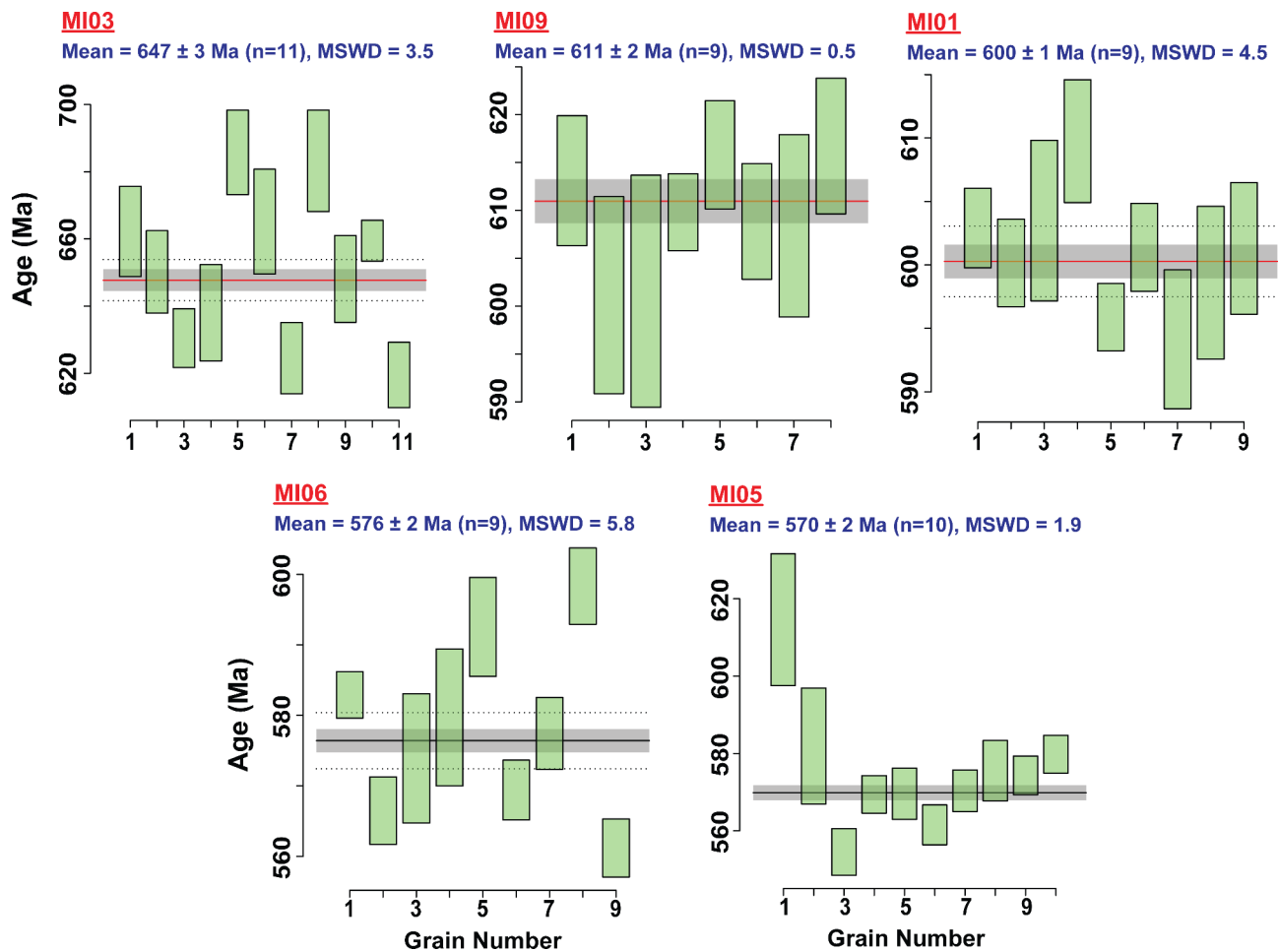
Fig. 7 Single zircon crystals U-Pb ages for samples within each sample populations

MI01). Afterwards, the last phase of the post-orogenic plutonism activated from 582±3 Ma (sample MI08) to 570±2 Ma (sample MI05). This suggests activation of the extensional tectonic regime in the studied region at 582±3 Ma, while this phase might have extended to 549±5 Ma as indicated by the grain B6 in sample MI08. The reworked nature of the Neoproterozoic crust in the ANS has been emphasized by the dating of some inherited grains with Pan-African ages (Table 4).

Additionally, rock suits classification based on their apparent chemical composition into Calc-alkaline "Grey" and Alkaline "Red" granitoids does not accurately capture the geological dynamics of the studied region, resulting in misleading interpretations of the chronological sequence and changes in the tectonic setting [2, 18–20]. Instead, the magma has differentiated from calc-alkaline to alkaline affinities over time [2, 19, 30].

Fig. 8 Concordia diagram for all zircon grains with discordance percent ≤ 10% for post-orogenic samples, plotted using IsopltR [121]

Table 4 LA-ICP-MS U-th-pb Zircon Data for the studied samples

| Sample Code | Gr. | Concentrations | | Age (Ma) and 2σ errors | | | | | | | | %discordance | Sample | |
		^{204}Pb	^{238}U	$^{206}Pb/$ ^{238}U	±2σ	$^{207}Pb/$ ^{235}U	±2σ	$^{207}Pb/$ ^{206}Pb	±2σ	Conc.	±2σ		Conc. (Ma)	±2σ
Island-arc														
MI10	A3	0.001	102	1207	12	1146	10	1032	10	1145	10	-5.3	729	3
	E5	0.009	173	1133	15	1145	14	1168	12	1146	13	1.1		
	E8	-0.003	181	1154	16	1159	14	1167	12	1159	14	0.4		
Syn-orogenic														
MI02	E2	0.003	337	1514	56	1545	53	1588	37	1549	4	2.0	699	4
	E8	-0.005	65	704	11	723	10	781	12	723	10	2.6		
MI11	C2	0.008	196	1042	29	1093	27	1194	24	1095	25	4.7	680	5
MI07	E3	-0.045	78	763	7	749	6	708	7	749	6	-1.8	646	2
Post-orogenic / Dokhan eruptions														
MI04	D3	0.002	101	579	6	594	5	648	7	594	5	2.4	623	2
Post-orogenic / Magmatic emplacements														
MI08	B4	0.006	165	740	10	762	9	772	13	762	9	2.9	582	3
	C7	0.000	128	606	7	621	6	629	14	621	6	2.4		
	B6	-0.001	102	555	6	549	5	556	15	549	5	-1.1		

More details are provided in the caption of Table 3.
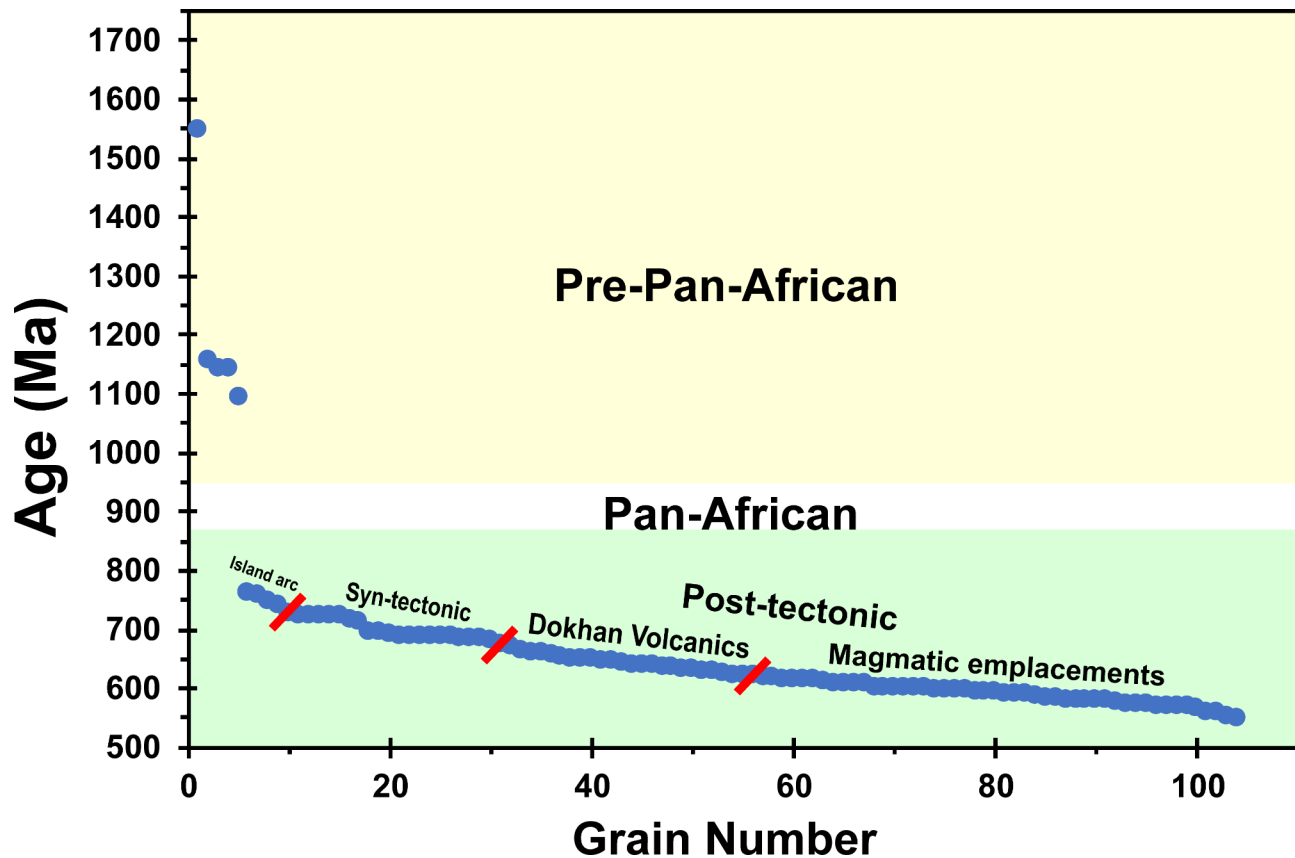
Fig. 9 Distribution chart for the analyzed single zircon U-Pb concordant ages from all samples

Conclusion

- The studied region in the CED was constructed through the island-arc, the syn-orogenic, and the post-orogenic magmatic phases (Fig. 9).

- The compressional regime of the arc-continent collision (the island-arc and syn-orogenic phases) was dominated between 729 ± 3 Ma and 646 ± 2 Ma in the CED.

- The Dokhan volcanism erupted during the tectonic transition setting between the subduction and the extension regimes from 623 ± 3 Ma to 600 ± 1 Ma.

- The post-collision tensional regime activated at 582 ± 3 Ma and may have extended to 549 ± 5 Ma.

- The reworked nature of the ANS plutonism has been emphasized by dating pre-Pan-African xenocrystic grains (Fig. 9).

- Classification of the ANS granitoids based on their chemical composition results in misleading interpretations of the chronological sequence and changes in the tectonic setting.

Author contributions
Conceptualization, S.M., R.H., and N.H.; methodology, S.M., A.T., and N.H.; validation, S.M., R.H., K.A., A.A.S., M.S.F., and N.H.; formal analysis, A.T., M.A.G., K.A., and S.M.; investigation, S.M., K.A., R.H., M.S.F., A.A.S., and N.H.; resources, N.H., M.S.F., and K.A.; data curation, S.M., A.A.S., and M.A.G.; writing—original draft preparation, S.M., R.H.; writing—review and editing, N.H., K.A., M.S.F., A.A.S., and M.A.G.; Visualization, S.M., K.A., M.S.F., and M.A.G.; project administration, R.H., S.M., A.T., K.A., and M.S.F.; funding acquisition, N.H., K.A., and M.S.F. All authors have read and agreed to the published version of the manuscript.

Data availability
No datasets were generated or analysed during the current study.

Declarations

Competing interests
The authors declare no competing interests.

Conflict of interest
The authors declare that the research was conducted in the absence of any commercial or financial relationships that could be construed as a potential conflict of interest.

Author details
[1]Geology Department, Faculty of Science, Port Said University, Port Said 42522, Egypt
[2]Institute of Nature and Environmental Technology, Kanazawa University, Kanazawa 920-1192, Japan
[3]Department of Geology & Geophysics, College of Science, King Saud University, Riyadh 11451, Saudi Arabia
[4]Faculty of Environmental Sciences, University of Diffa, Diffa, Niger
[5]Department of Earth Sciences, Kanazawa University, Kanazawa 920-1192, Japan

References
1. Be'eri-Shlevin Y, Eyal M, Eyal Y et al (2012) The Sa'al volcano-sedimentary complex (Sinai, Egypt): a latest Mesoproterozoic volcanic arc in the northern Arabian Nubian Shield. Geology 40:403–406. https://doi.org/10.1130/G32788.1
2. Mansour S, Hasebe N, Meert JG et al (2022) Evolution of the Arabian-Nubian Shield in Gabal Samra area, Sinai; implications from zircon U–Pb geochronology. J Afr Earth Sc 192:104538. https://doi.org/10.1016/j.jafrearsci.2022.104538
3. Mansour S, Hasebe N, Tamura A (2023) Erosional reservoir for the northern segment of the arabian-nubian shield: constrains from U-Pb geochronology of the lower palaeozoic succession, North Eastern Desert, Egypt. Precambrian Res 388:107017. https://doi.org/10.1016/j.precamres.2023.107017
4. El-Gaby S, El-Nady O, Khudeir A (1984) Tectonic evolution of the basement complex in the central eastern desert of Egypt. Geol Rundsch 73:1019–1036. https://doi.org/10.1007/BF01820886
5. El-Bialy MZ (2021) The Ediacaran Post-collisional Dokhan Volcanics. In: Hamimi Z, Arai S, Fowler A-R, El-Bialy MZ (eds) The geology of the Egyptian Nubian Shield. Springer International Publishing, Cham, pp 267–294
6. Eliwa HA, Kimura J-I, Itaya T (2006) Late neoproterozoic Dokhan Volcanics, North Eastern Desert, Egypt: Geochemistry and petrogenesis. Precambrian Res 151:31–52. https://doi.org/10.1016/j.precamres.2006.08.005
7. Adam MMA, Lv X, Fathy D et al (2022) Petrogenesis and tectonic implications of Tonian island arc volcanic rocks from the Gabgaba Terrane in the Arabian-Nubian Shield (NE Sudan). J Asian Earth Sci 223:105006. https://doi.org/10.1016/j.jseaes.2021.105006
8. Ali KA, Wilde SA, Stern RJ et al (2013) Hf isotopic composition of single zircons from neoproterozoic arc volcanics and post-collision granites, Eastern Desert of Egypt: implications for crustal growth and recycling in the Arabian-Nubian Shield. Precambrian Res 239:42–55. https://doi.org/10.1016/j.precamres.2013.05.007
9. Abd El-Rahman Y, Polat A, Dilek Y et al (2009) Geochemistry and tectonic evolution of the neoproterozoic incipient arc–forearc crust in the Fawakhir area, Central Eastern Desert of Egypt - ScienceDirect. Precambrian Res 175:116–134
10. Meert JG (2003) A synopsis of events related to the assembly of eastern Gondwana. Tectonophysics 362:1–40. https://doi.org/10.1016/S0040-1951(02)00629-7
11. Stern RJ (2008) Neoproterozoic crustal growth: the solid earth system during a critical episode of Earth history. Gondwana Res 14:33–50. https://doi.org/10.1016/j.gr.2007.08.006
12. Stern RJ (2005) Evidence from ophiolites, blueschists, and ultrahigh-pressure metamorphic terranes that the modern episode of subduction tectonics began in neoproterozoic time. Geol 33:557. https://doi.org/10.1130/G21365.1
13. Fowler A-R, Hamimi Z (2020) Structural and tectonic Framework of Neoproterozoic basement of Egypt: from Gneiss domes to Transpression Belts. In: Hamimi Z, El-Barkooky A, Martínez Frías J et al (eds) The geology of Egypt. Springer International Publishing, Cham, pp 81–129
14. Ries AC, Shackleton RM, Graham RH, Fitches WR (1983) Pan-african structures, ophiolites and mélange in the Eastem Desert of Egypt: a traverse at 26°N. J Geol Soc 140:75–95. https://doi.org/10.1144/gsjgs.140.1.0075
15. El Ramly MF, Akaad MK (1960) The basement complex in the Central-Eastern Desert of Egypt between Lat. 24°30 and 25° 40 N. Geol Surv Egypt Annals 8:1–35
16. Schurmann HME (1953) The Precambrian of the Gulf of Suez area. Int Geol Congr Algiers CR 19:115–135
17. Hume WF (1935) The later plutonic and minor intrusive rocks. Survey of Egypt, Cairo
18. Moreno JA, Montero P, Abu Anbar M et al (2012) SHRIMP U–Pb zircon dating of the Katerina Ring Complex: insights into the temporal sequence of Ediacaran calc-alkaline to peralkaline magmatism in southern Sinai, Egypt. Gondwana Res 21:887–900. https://doi.org/10.1016/j.gr.2011.08.010
19. Ali BH, Wilde SA, Gabr MMA (2009) Granitoid evolution in Sinai, Egypt, based on precise SHRIMP U–Pb zircon geochronology. Gondwana Res 15:38–48. https://doi.org/10.1016/j.gr.2008.06.009
20. Be'eri-Shlevin Y, Katzir Y, Whitehouse MJ (2009) Post-collisional tectonomagmatic evolution in the northern Arabian–Nubian Shield: time constraints from ion-probe U–Pb dating of zircon. J Geol Soc 166:71–85. https://doi.org/10.1144/0016-76492007-169
21. Abdelfadil KM, Mansour S, Asran AM et al (2024) Composite Granitic Plutonism in the Southern Part of the Wadi Hodein Shear Zone, South Eastern Desert, Egypt: implications for neoproterozoic dioritic and highly evolved Magma Mingling during volcanic Arc Assembly. Minerals 14:1002. https://doi.org/10.3390/min14101002
22. Stern RJ, Hedge CE (1985) Geochronologic and isotopic constraints on late precambrian crustal evolution in the Eastern Desert of Egypt. Am J Sci 285:97. https://doi.org/10.2475/ajs.285.2.97
23. Abu El-Enen MM, Whitehouse MJ (2013) The feiran–solaf metamorphic complex, Sinai, Egypt: Geochronological and geochemical constraints on its evolution. Precambrian Res 239:106–125. https://doi.org/10.1016/j.precamres.2013.10.011
24. Breitkreuz C, Eliwa H, Khalaf I et al (2010) Neoproterozoic SHRIMP U–Pb zircon ages of silica-rich Dokhan Volcanics in the North Eastern Desert, Egypt. Precambrian Res 182:163–174. https://doi.org/10.1016/j.precamres.2010.06.019
25. Wilde Simona, Youssef K (2002) A re-evaluation of the origin and setting of the late precambrian Hammamat Group based on SHRIMP U–Pb dating of detrital zircons from Gebel Umm Tawat, North Eastern Desert, Egypt. J Geol Soc 159:595–604. https://doi.org/10.1144/0016-764901-081
26. Hume WF (1934) Geology of Egypt, V. II, Part II, the later plutonic and minor intrusive rocks. Geological Survey of Egypt, Cairo V
27. Schürmann HME (1966) The pre-cambrian along the Gulf of Suez and the northern part of the Red Sea, 1st edn. G.J. Brill, Leiden
28. Shimron AE (1980) Proterozoic island arc volcanism and sedimentation in Sinai. Precambrian Res 12:437–458. https://doi.org/10.1016/0301-9268(80)90039-X
29. Abdel-Khalek ML, Takla MA, Sehim A et al (1992) Geology and tectonic evolution of Wadi Beitan area, Southeastern Desert, Egypt. In: Sadek A (ed) Geo. of the Arab World. Cairo University, pp 369–394
30. Moussa EMM, Stern RJ, Manton WI, Ali KA (2008) SHRIMP zircon dating and Sm/Nd isotopic investigations of neoproterozoic granitoids, Eastern Desert, Egypt. Precambrian Res 160:341–356. https://doi.org/10.1016/j.precamres.2007.08.006
31. Stern RJ, Manton WI (1987) Age of Feiran basement rocks, Sinai: implications for late precambrian crustal evolution in the northern arabian–nubian Shield. J Geol Soc 144:569–575. https://doi.org/10.1144/gsjgs.144.4.0569
32. Kröner A, Eyal M, Eyal Y (1990) Early pan-african evolution of the basement around Elat, Israel,and the Sinai Peninsula revealed by single-zircon evaporation dating, and implications for crustal accretion rates. Geology 18:545–548. https://doi.org/10.1130/0091-7613(1990)018<0545:EPAEOT>2.3.CO;2
33. Eyal M, Be'eri-Shlevin Y, Eyal Y et al (2014) Three successive proterozoic island arcs in the Northern Arabian–Nubian Shield: evidence from SIMS U–Pb dating of zircon. Gondwana Res 25:338–357. https://doi.org/10.1016/j.gr.2013.03.016
34. Mansour S, Hasebe N, Azab E et al (2021) Combined Zircon/Apatite U-Pb and fission-track dating by LA-ICP-MS and its geological applications: an Example from the Egyptian younger granites. Minerals 11:1341. https://doi.org/10.3390/min11121341
35. Andresen A, El-Rus MAA, Myhre PI et al (2009) U–Pb TIMS age constraints on the evolution of the Neoproterozoic Meatiq Gneiss Dome, Eastern Desert, Egypt. Int J Earth Sci (Geol Rundsch) 98:481–497. https://doi.org/10.1007/s00531-007-0276-x
36. Stern RJ, Khedr MZ, Whitehouse MJ et al (2023) Late cryogenian and early ediacaran rare metal-rich granites in the Eastern Desert of Egypt: constraints from zircon ages and whole-rock Sr- and Nd- and feldspar Pb- isotopic compositions. J Geol Soc 0:jgs2023-068. https://doi.org/10.1144/jgs2023-068
37. Abo Khashaba S, El-Shibiny NH, Hassan S et al (2023) Application of remote sensing data integration in detecting mineralized granitic zones: a case study

of the Gabal Al-Ijlah Al-Hamra, Central Eastern Desert, Egypt. J Afr Earth Sc 200:104855. https://doi.org/10.1016/j.jafrearsci.2023.104855

38. Khedr MZ, Abo Khashaba SM, El-Shibiny NH et al (2022) Remote sensing techniques and geochemical constraints on the formation of the Wadi El-Hima mineralized granites, Egypt: new insights into the genesis and accumulation of garnets. Int J Earth Sci (Geol Rundsch) 111:2409–2443. https://doi.org/10.1007/s00531-022-02237-7

39. Mansour S (2015) Long-term topographic evolution of the African plate, causes and consequences for surrounding lithospheric plates. Universität Heidelberg

40. Ali KA, Azer MK, Gahlan HA et al (2010) Age constraints on the formation and emplacement of neoproterozoic ophiolites along the allaqi–heiani suture, South Eastern Desert of Egypt. Gondwana Res 18:583–595. https://doi.org/10.1016/j.gr.2010.03.002

41. El-Bialy MZ (2020) Precambrian basement complex of Egypt. In: Hamimi Z, El-Barkooky A, Martínez Frías J et al (eds) The geology of Egypt. Springer International Publishing, Cham, pp 37–79

42. Mohammad AT, El Kazzaz YA, Hassan SM, Taha MMN (2020) Neoproterozoic tectonic evolution and exhumation history of transpressional shear zones in the east African orogen: implications from kinematic analysis of Meatiq area, Central Eastern Desert of Egypt. Int J Earth Sci (Geol Rundsch) 109:253–279. https://doi.org/10.1007/s00531-019-01801-y

43. Lundmark AM, Andresen A, Hassan MA et al (2012) Repeated magmatic pulses in the East African Orogen in the Eastern Desert, Egypt: an old idea supported by new evidence. Gondwana Res 22:227–237. https://doi.org/10.1016/j.gr.2011.08.017

44. Youssef KM (2005) The age and petrogenesis of the major rock units at Gabal Gattar and Gabal El Dokhan, Northeastern Desert, Egypt. PhD Thesis, Curtin University of Technology

45. Hassan MA, Hashad AH (1990) Precambrian of Egypt. In: Said R (ed) Geology of Egypt, 2nd edn. Balkema, Netherlands, p 734

46. Stampfli GM, von Raumer JF, Borel GD (2002) Paleozoic evolution of pre-variscan terranes: from Gondwana to the Variscan collision. Variscan-Appalachian dynamics: the building of the late paleozoic basement. Geological Society of America, Boulder, USA

47. Sakran S, Shehata AA, Osman O, El-Sherbiny M (2019) Superposed tectonic regimes in west Beni Suef Basin, Nile Valley, Egypt: implications to source rock maturation and hydrocarbon entrapment. J Afr Earth Sc 154:1–19. https://doi.org/10.1016/j.jafrearsci.2019.03.010

48. Shehata AA, El Fawal FM, Ito M et al (2020) Senonian platform-to-slope evolution in the tectonically-influenced Syrian Arc sedimentary belt: Beni Suef Basin, Egypt - ScienceDirect. J Afr Earth Sc 170. https://doi.org/10.1016/j.jafrearsci.2020.103934

49. Mansour S, Hasebe N, Abdelrahman K et al (2023) Reconstructing the Tectonic history of the Arabian–Nubian Shield in Sinai: low-temperature thermochronology implications on Wadi Agar Area. Minerals 13:574. https://doi.org/10.3390/min13040574

50. Mansour S, Gharib MA, Hasebe N et al (2023) Tectonic evolution of the Gabal Loman area, North Eastern Desert, Egypt: implications from low-temperature multithermochronometry on the arabian-nubian shield. Front Earth Sci 11:15. https://doi.org/10.3389/feart.2023.1193692

51. Mansour S, Hasebe N, Khedr MZ et al (2023) Tectonic-thermal evolution of the Wadi El-Dahal Area, North Eastern Desert, Egypt: constraints on the Suez Rift Development. Minerals 13:1021. https://doi.org/10.3390/min13081021

52. Mansour S, Hasebe N, Abdelrahman K et al (2024) The Gulf of Suez rifting: implications from low-temperature thermochronology. Int Geol Rev 1–17. https://doi.org/10.1080/00206814.2024.2400695

53. Kennedy WQ (1964) The structural differentiation of Africa in the pan-african (± 500 m.y.) tectonic episode. Leeds Univ Res Inst Afr Geol Department Earth Sci Annual Rep Sci Results 8:48–49

54. Kröner A, Todt W, Hussein I et al (1992) Dating of late proterozoic ophiolites in Egypt and the Sudan using the single grain zircon evaporation technique. Precambrian Res 59:15–32. https://doi.org/10.1016/0301-9268(92)90049-T

55. Engel AEJ, Dixon TH, Stern RJ (1980) Late precambrian evolution of afro-arabian crust from ocean arc to craton. GSA Bull 91:699. https://doi.org/10.1130/0016-7606(1980)91<699:LPEOAC>2.0.CO;2

56. Fleck RJ, Greenwood WR, Hadley DG et al (1980) Professional Paper

57. Gass IG (1981) Chap. 15 pan-african (Upper Proterozoic) plate tectonics of the Arabian—Nubian Shield. In: developments in Precambrian Geology. Elsevier, pp 387–405

58. Johnson PR (2014) An expanding Arabian-Nubian Shield geochronologic and isotopic dataset: defining limits and confirming the tectonic setting of a neoproterozoic accretionary orogen. Open Geol J 3–33

59. Meert JG, Van Der Voo R (1997) The assembly of Gondwana 800 – 550 ma. J Geodyn 23:223–235. https://doi.org/10.1016/S0264-3707(96)00046-4

60. Stern RJ (1994) ARC Assembly and Continental Collision in the Neoproterozoic East African Orogen: implications for the consolidation of Gondwana-land. Annu Rev Earth Planet Sci 22:319–351. https://doi.org/10.1146/annurev.ea.22.050194.001535

61. Mahdy NM, Ntaflos T, Pease V et al (2020) Combined zircon U-Pb dating and chemical Th–U–total pb chronology of monazite and thorite, Abu Diab A-type granite, Central Eastern Desert of Egypt: constraints on the timing and magmatic-hydrothermal evolution of rare metal granitic magmatism in the Arabian Nubian Shield. Geochemistry 80:125669. https://doi.org/10.1016/j.chemer.2020.125669

62. Andresen A, Abu El-Enen MM, Stern RJ et al (2014) The Wadi Zaghra metasediments of Sinai, Egypt: new constraints on the late cryogenian–ediacaran tectonic evolution of the northernmost arabian–nubian Shield. Int Geol Rev 56:1020–1038. https://doi.org/10.1080/00206814.2014.907755

63. Eliwa HA, El-Bialy MZ, Murata M (2014) Edicaran post-collisional volcanism in the Arabian-Nubian Shield: the high-K calc-alkaline Dokhan Volcanics of Gabal Samr El-Qaa (592 ± 5 ma), North Eastern Desert, Egypt. Precambrian Res 246:180–207. https://doi.org/10.1016/j.precamres.2014.03.015

64. Eyal M, Litvinovsky B, Jahn BM et al (2010) Origin and evolution of post-collisional magmatism: Coeval Neoproterozoic calc-alkaline and alkaline suites of the Sinai Peninsula. Chem Geol 269:153–179. https://doi.org/10.1016/j.chemgeo.2009.09.010

65. Fowler A-R, Hamimi Z (2023) Lithospheric delamination in models of post-collision tectonics in the Egyptian Eastern Desert and Sinai: claims versus evidence. J Afr Earth Sc 203:104948. https://doi.org/10.1016/j.jafrearsci.2023.104948

66. Johnson PR, Andresen A, Collins AS et al (2011) Late cryogenian–ediacaran history of the Arabian–Nubian Shield: a review of depositional, plutonic, structural, and tectonic events in the closing stages of the northern East African Orogen. J Afr Earth Sc 61:167–232. https://doi.org/10.1016/j.jafrearsci.2011.07.003

67. El-Bialy MZ, Hassen IS (2012) The late Ediacaran (580–590 ma) onset of anorogenic alkaline magmatism in the Arabian–Nubian Shield: Katherina A-type rhyolites of Gabal Ma'ain, Sinai, Egypt. Precambrian Res 216–219:1–22. https://doi.org/10.1016/j.precamres.2012.06.004

68. Obeid MA, Azer MK (2015) Pan-african adakitic rocks of the north arabian–nubian Shield: petrological and geochemical constraints on the evolution of the Dokhan volcanics in the north Eastern Desert of Egypt. Int J Earth Sci 104:541–563. https://doi.org/10.1007/s00531-014-1103-9

69. Maurice AE, Bakhit BR, Basta FF et al (2018) The last subduction-related volcanism in the northern tip of the Arabian-Nubian Shield: a neoproterozoic arc preceding the terminal collision of East and West Gondwana. Precambrian Res 310:256–277. https://doi.org/10.1016/j.precamres.2018.03.009

70. Khalaf E (2012) Origin and evolution of post-collisional volcanism: an example from Neoproterozoic Dokhan volcanics at Gabal Nugara area, Northeastern Desert, Egypt. Arabian Journal of Geosciences -. ARAB J GEOSCI 5:1–33. https://doi.org/10.1007/s12517-010-0242-y

71. Moghazi AM (2003) Geochemistry and petrogenesis of a high-K calc-alkaline Dokhan volcanic suite, South Safaga area, Egypt: the role of late neoproterozoic crustal extension. Precambrian Res 125:161–178. https://doi.org/10.1016/S0301-9268(03)00110-4

72. Abdel-Rahman A-FM (1996) Pan-african volcanism: petrology and geochemistry of the Dokhan Volcanic suite in the northern nubian shield. Geol Mag 133:17–31. https://doi.org/10.1017/S0016756800007226

73. Abdelfadil KM, Obeid MA, Azer MK, Asimow PD (2018) Late neoproterozoic adakitic lavas in the arabian-nubian shield, Sinai Peninsula, Egypt. J Asian Earth Sci 158:301–323. https://doi.org/10.1016/j.jseaes.2018.02.018

74. Mohamed FH, Moghazi AM, Hassanen MA (2000) Geochemistry, petrogenesis and tectonic setting of late neoproterozoic dokhan-type volcanic rocks in the Fatira area, eastern Egypt. Int J Earth Sci 88:764–777. https://doi.org/10.1007/s005310050304

75. Abu El-Enen MM, Abu-Alam TS, Whitehouse MJ et al (2016) P–T path and timing of crustal thickening during amalgamation of East and West Gondwana: a case study from the Hafafit Metamorphic Complex, Eastern Desert of Egypt. Lithos 263:213–238. https://doi.org/10.1016/j.lithos.2016.01.001

76. Ressetar R, Monrad JR (1983) Chemical composition and tectonic setting of the Dokhan Volcanic Formation, Eastern Desert, Egypt.

Journal of African Earth Sciences (1983) 1:103–112. https://doi.org/10.1016/0899-5362(83)90002-7

77. Azer MK, Farahat ES (2011) Late neoproterozoic volcano-sedimentary successions of Wadi Rufaiyil, southern Sinai, Egypt: a case of transition from late- to post-collisional magmatism. J Asian Earth Sci 42:1187–1203. https://doi.org/10.1016/j.jseaes.2011.06.016

78. Abdelkareem M, Hamimi Z, El-Bialy MZ et al (2021) Integration of remote-sensing data for mapping lithological and structural features in the Esh El-Mallaha area, West Gulf of Suez, Egypt. Arab J Geosci 14:497. https://doi.org/10.1007/s12517-021-06791-3

79. El-Bialy MZ, Shata AE (2018) Geochemistry, petrogenesis and radioactive mineralization of two coeval neoproterozoic post-collisional calc-alkaline and alkaline granitoid suites from Sinai, Arabian Nubian Shield. Geochemistry 78:15–39. https://doi.org/10.1016/j.chemer.2017.12.001

80. Fritz H, Abdelsalam M, Ali KA et al (2013) Orogen styles in the East African Orogen: a review of the neoproterozoic to Cambrian tectonic evolution. J Afr Earth Sc 86:65–106. https://doi.org/10.1016/j.jafrearsci.2013.06.004

81. Bregar M, Bauernhofer A, Pelz K et al (2002) A late neoproterozoic magmatic core complex in the Eastern Desert of Egypt: emplacement of granitoids in a wrench-tectonic setting. Precambrian Res 118:59–82. https://doi.org/10.1016/S0301-9268(02)00062-1

82. Fowler TJ, Osman AF (2001) Gneiss-cored interference dome associated with two phases of late pan-african thrusting in the Central Eastern Desert, Egypt. Precambrian Res 108:17–43. https://doi.org/10.1016/S0301-9268(00)00146-7

83. Fritz H, Wallbrecher E, Khudeir AA et al (1996) Formation of neoproterozoic metamorphic complex during oblique convergence (Eastern Desert, Egypt). J Afr Earth Sc 23:311–329. https://doi.org/10.1016/S0899-5362(97)00004-3

84. Greiling RO, Abdeen MM, Dardir AA et al (1994) A structural synthesis of the Proterozoic Arabian-Nubian Shield in Egypt. Geol Rundsch 83:484–501. https://doi.org/10.1007/BF01083222

85. Fritz H, Dallmeyer DR, Wallbrecher E et al (2002) Neoproterozoic tectonothermal evolution of the Central Eastern Desert, Egypt: a slow velocity tectonic process of core complex exhumation. J Afr Earth Sc 34:137–155. https://doi.org/10.1016/S0899-5362(02)00014-3

86. Shalaby A, Stuwe K, Makroum F et al (2005) The Wadi Mubarak belt, Eastern Desert of Egypt: a neoproterozoic conjugate shear system in the Arabian?Nubian Shield. Precambrian Res 136:27–50. https://doi.org/10.1016/j.precamres.2004.09.005

87. Loizenbauer J (2001) Structural geology, single zircon ages and fluid inclusion studies of the Meatiq metamorphic core complex: implications for neoproterozoic tectonics in the Eastern Desert of Egypt. Precambrian Res 110:357–383. https://doi.org/10.1016/S0301-9268(01)00176-0

88. Kröner A (1985) Ophiolites and the evolution of tectonic boundaries in the late proterozoic arabian—nubian shield of northeast Africa and Arabia. Precambrian Res 27:277–300. https://doi.org/10.1016/0301-9268(85)90016-6

89. El-Sayed MM, Furnes H, Shagar SA (2007) Growth of the Egyptian crust in the northern East African Orogen: a review of existing models and proposed modifications. Neues Jahrbuch für Mineralogie - Abhandlungen 317–341. https://doi.org/10.1127/0077-7757/2007/0078

90. Akaad MK, Noweir AM (1980) Geology and Lithostratigraphy of the arabian Desert Orogenic Belt of Egypt between Lat. 25° 35′ and 26° 30′N. Bull Inst Appl Geo Jeddah 4:127–134

91. Hussein AAA, Ali MM, El Ramly MF (1982) A proposed new classification of the granites of Egypt. J Volcanol Geoth Res 14:187–198. https://doi.org/10.1016/0377-0273(82)90048-8

92. El Shazly EM (1964) On the classification of the Precambrian and other rocks of magmatic affiliation in Egypt. n: Proc 22nd Intl Geol Congr, New Delhi 88–101

93. Abd El-Wahed MA (2014) Oppositely dipping thrusts and transpressional imbricate zone in the Central Eastern Desert of Egypt. J Afr Earth Sc 100:42–59. https://doi.org/10.1016/j.jafrearsci.2014.06.010

94. Fowler A-R, Khamees H, Dowidar H (2007) El Sibai gneissic complex, Central Eastern Desert, Egypt: folded nappes and syn-kinematic gneissic granitoid sheets – not a core complex. J Afr Earth Sc 49:119–135. https://doi.org/10.1016/j.jafrearsci.2007.08.004

95. Augland LE, Andresen A, Boghdady GY (2012) U–Pb ID-TIMS dating of igneous and metaigneous rocks from the El-Sibai area: time constraints on the tectonic evolution of the Central Eastern Desert, Egypt. Int J Earth Sci 101:25–37. https://doi.org/10.1007/s00531-011-0653-3

96. Andresen A, Augland LE, Boghdady GY et al (2010) Structural constraints on the evolution of the Meatiq Gneiss Dome (Egypt), East-African Orogen. J Afr Earth Sc 57:413–422. https://doi.org/10.1016/j.jafrearsci.2009.11.007

97. Zoheir B, Goldfarb R, Holzheid A et al (2020) Geochemical and geochronological characteristics of the Um Rus granite intrusion and associated gold deposit, Eastern Desert, Egypt. Geosci Front 11:325–345. https://doi.org/10.1016/j.gsf.2019.04.012

98. Tamura A, Sagawa T, Okino K, Morishita T (2022) Determination of whole-rock trace-element compositions of siliceous rocks using MgO-diluted fused glass and LA-ICP-MS. Geochem J 56:231–239. https://doi.org/10.2343/geochemj.GJ22020

99. Jeffries TE, Pearce NJG, Perkins WT, Raith A (1996) Chemical fractionation during infrared and ultraviolet laser ablation inductively coupled plasma mass spectrometry—implications for mineral microanalysis. Anal Commun 33:35–39. https://doi.org/10.1039/AC9963300035

100. Horn I, Rudnick RL, McDonough WF (2000) Precise elemental and isotope ratio determination by simultaneous solution nebulization and laser ablation-ICP-MS: application to U–Pb geochronology. Chem Geol 164:281–301. https://doi.org/10.1016/S0009-2541(99)00168-0

101. Hirata T, Nesbitt RW (1995) U-Pb isotope geochronology of zircon: evaluation of the laser probe-inductively coupled plasma mass spectrometry technique. Geochim Cosmochim Acta 59:2491–2500. https://doi.org/10.1016/0016-7037(95)00144-1

102. Jackson SE, Pearson NJ, Griffin WL, Belousova EA (2004) The application of laser ablation-inductively coupled plasma-mass spectrometry to in situ U–Pb zircon geochronology. Chem Geol 211:47–69. https://doi.org/10.1016/j.chemgeo.2004.06.017

103. Poitrasson F, Chenery S, Shepherd TJ (2000) Electron microprobe and LA-ICP-MS study of monazite hydrothermal alteration. Geochim Cosmochim Acta 64:3283–3297. https://doi.org/10.1016/S0016-7037(00)00433-6

104. Lin J, Liu Y, Yang Y, Hu Z (2016) Calibration and correction of LA-ICP-MS and LA-MC-ICP-MS analyses for element contents and isotopic ratios. Solid Earth Sci 1:5–27. https://doi.org/10.1016/j.sesci.2016.04.002

105. Eggins SM, Shelley JMG (2002) Compositional heterogeneity in NIST SRM 610–617 glasses. Geostandards Newsl 26:269–286. https://doi.org/10.1111/j.1751-908X.2002.tb00634.x

106. Arevalo R Jr, McDonough WF, Piccoli PM (2011) In situ determination of first-row transition metal, Ga and Ge abundances in Geological materials via Medium-Resolution LA-ICP-MS. Geostand Geoanal Res 35:253–273. https://doi.org/10.1111/j.1751-908X.2010.00099.x

107. Hu Z, Liu Y, Chen L et al (2011) Contrasting matrix induced elemental fractionation in NIST SRM and rock glasses during laser ablation ICP-MS analysis at high spatial resolution. J Anal Spectrom 26:425–430. https://doi.org/10.1039/C0JA00145G

108. Jochum K, Stoll B, Herwig K, Willbold M (2007) Validation of LA-ICP-MS trace element analysis of geological glasses using a new solid-state 193 nm Nd: YAG laser and matrix-matched calibration. Journal of Analytical Atomic Spectrometry, v22, 112–121 (2007) 22:. https://doi.org/10.1039/B609547J

109. Liu Y, Hu Z, Gao S et al (2008) In situ analysis of major and trace elements of anhydrous minerals by LA-ICP-MS without applying an internal standard. Chem Geol 257:34–43. https://doi.org/10.1016/j.chemgeo.2008.08.004

110. Bertini M, Izmer A, Vanhaecke F, Krupp EM (2013) Critical evaluation of quantitative methods for the multi-elemental analysis of ancient glasses using laser ablation inductively coupled plasma mass spectrometry. J Anal Spectrom 28:77–91. https://doi.org/10.1039/C2JA30036B

111. Günther D, Jackson SE, Longerich HP (1999) Laser ablation and arc/spark solid sample introduction into inductively coupled plasma mass spectrometers. Spectrochimica Acta Part B: at Spectrosc 54:381–409. https://doi.org/10.1016/S0584-8547(99)00011-7

112. Longerich HP, Jackson SE, Günther D (1996) Inter-laboratory note. Laser ablation inductively coupled plasma mass spectrometric transient signal data acquisition and analyte concentration calculation. J Anal Spectrom 11:899–904. https://doi.org/10.1039/JA9961100899

113. Mukherjee PK, Khanna PP, Saini NK (2014) Rapid Determination of Trace and Ultra Trace Level Elements in Diverse Silicate Rocks in pressed powder pellet targets by LA-ICP-MS using a matrix-independent protocol. Geostand Geoanal Res 38:363–379. https://doi.org/10.1111/j.1751-908X.2013.00260.x

114. Perkins WT, Pearce NJG, Westgate JA (1997) The development of laser ablation ICP-MS and calibration strategies: examples from the analysis of Trace Elements in Volcanic Glass shards and Sulfide minerals. Geostandards Newsl 21:175–190. https://doi.org/10.1111/j.1751-908X.1997.tb00669.x

115. Paces JB, Miller JD (1993) Precise U-Pb ages of Duluth Complex and related mafic intrusions, northeastern Minnesota: geochronological insights to physical, petrogenetic, paleomagnetic, and tectonomagmatic processes

associated with the 1.1 Ga Midcontinent Rift System. J Geophys Res 98:13997–14013. https://doi.org/10.1029/93JB01159

116. Sláma J, Košler J, Condon DJ et al (2008) Plešovice zircon — a new natural reference material for U–Pb and hf isotopic microanalysis. Chem Geol 249:1–35. https://doi.org/10.1016/j.chemgeo.2007.11.005

117. Schoene B, Crowley JL, Condon DJ et al (2006) Reassessing the uranium decay constants for geochronology using ID-TIMS U–Pb data. Geochim Cosmochim Acta 70:426–445. https://doi.org/10.1016/j.gca.2005.09.007

118. Pearce NJG, Perkins WT, Westgate JA et al (1997) Geostand Geoanal Res 21:115–144. https://doi.org/10.1111/j.1751-908X.1997.tb00538.x. A Compilation of New and Published Major and Trace Element Data for NIST SRM 610 and NIST SRM 612 Glass Reference Materials

119. Carpenter BS, Reimer GM (1974) Standard reference materials: calibrated glass standards for fission track use

120. Guillong M, Von Quadt A, Sakata S et al (2014) LA-ICP-MS Pb–U dating of young zircons from the Kos–Nisyros volcanic centre, SE Aegean arc. J Anal Spectrom 29:963–970. https://doi.org/10.1039/C4JA00009A

121. Vermeesch P (2018) IsoplotR: a free and open toolbox for geochronology. Geosci Front 9:1479–1493. https://doi.org/10.1016/j.gsf.2018.04.001

122. Rubatto D (2017) Zircon: the Metamorphic Mineral. Rev Mineral Geochem 83:261–295. https://doi.org/10.2138/rmg.2017.83.9

123. Rubatto D (2002) Zircon trace element geochemistry: partitioning with garnet and the link between U–Pb ages and metamorphism. Chem Geol 184:123–138. https://doi.org/10.1016/S0009-2541(01)00355-2

124. Awad HA, Zakaly HMH, Nastavkin AV et al (2021) Radioactive mineralizations on granitic rocks and silica veins on shear zone of El-Missikat area, Central Eastern Desert, Egypt. Appl Radiat Isot 168:109493. https://doi.org/10.1016/j.apradiso.2020.109493

125. Murphy JB, FernÁndez-SuÁrez J, Jeffries TE, Strachan RA (2004) U–Pb (LA–ICP-MS) dating of detrital zircons from Cambrian clastic rocks in Avalonia: erosion of a neoproterozoic arc along the northern Gondwanan margin. J Geol Soc 161:243–254. https://doi.org/10.1144/0016-764903-064

126. Moghazi A-KM (1999) Magma source and evolution of late neoproterozoic granitoids in the Gabal El-Urf area, Eastern Desert, Egypt: geochemical and Sr–Nd isotopic constraints. Geol Mag 136:285–300. https://doi.org/10.1017/S0016756899002563

127. Platt JP, England PC (1994) Convective removal of lithosphere beneath mountain belts; thermal and mechanical consequences. Am J Sci 294:307–336. https://doi.org/10.2475/ajs.294.3.307

128. Stern RJ, Ali KA, Liégeois JP et al (2010) Distribution and significance of pre-neoproterozoic zircons in Juvenile Neoproterozoic Igneous rocks of the Arabian-Nubian Shield. Am J Sci 310:791–811. https://doi.org/10.2475/09.2010.02

129. Stern RJ, Johnson PR, Kröner A, Yibas B (2004) Neoproterozoic ophiolites of the Arabian-Nubian Shield. Developments in Precambrian Geology. Elsevier, pp 95–128

130. Dilek Y, Ahmed Z (2003) Proterozoic ophiolites of the Arabian Shield and their significance in precambrian tectonics. SP 218:685–700. https://doi.org/10.1144/GSL.SP.2003.218.01.33

131. Azer MK, Stern RJ (2007) Neoproterozoic (835–720 ma) serpentinites in the Eastern Desert, Egypt: fragments of Forearc Mantle. J Geol 115:457–472. https://doi.org/10.1086/518052

132. Goscombe BD, Gray DR (2008) Structure and strain variation at mid-crustal levels in a transpressional orogen: a review of Kaoko Belt structure and the character of West Gondwana amalgamation and dispersal. Gondwana Res 13:45–85. https://doi.org/10.1016/j.gr.2007.07.002

133. Abd El-Wahed M, Hamimi Z (2021) The Egyptian Nubian Shield Within the Frame of the Arabian–Nubian Shield. In: Hamimi Z, Arai S, Fowler AR, El-Bialy MZ (eds) The Geology of the Egyptian Nubian Shield, Regional Geology Reviews, 1st ed. Springer, pp 15–51

134. Kröner A, Kröger J, Rashwan AAA (1994) Age and tectonic setting of granitoid gneisses in the Eastern Desert of Egypt and south-west Sinai. Geol Rundsch 83:502–513. https://doi.org/10.1007/BF00194157

135. Bar M, Kolodny Y, Bentor YK (1974) Dating faults by fission track dating of epidotes — an attempt. Earth Planet Sci Lett 22:157–162. https://doi.org/10.1016/0012-821X(74)90076-4

136. Bielski M, Jäger E, Steinitz G (1979) The geochronology of lqna Granite (wadi kid pluton), Southern Sinai. Contr Mineral Petrol 70:159–165. https://doi.org/10.1007/BF00374445

Publisher's note